Simulation of Cold Jet Installation Noise using a Stochastic Backscatter Model

Roland Ewert,[*] Jürgen Dierke,[†] Andrej Neifeld[‡]

Institute of Aerodynamics and Flow Technology, Technical Acoustics

German Aerospace Center (DLR)

Lilienthalplatz 7, 381208 Braunschweig, Germany

This work presents first results obtained with partly scale resolving simulation for two different installation noise problems involving a cold jet interacting with a wing. Similar to very large-eddy simulation (VLES), the resolvable very large scales of turbulent fluctuations are directly calculated and the dissipation of the non-resolved scales is accounted for by a subfilter scale stress model. In addition, stochastic forcing in space and time is applied to model turbulent backscatter. The paper presents and discusses the rationale to explicitly realize turbulent backscatter along with details of the proposed stochastic backscatter model and its calibration. As a novel approach, the entire subfilter forcing function is modeled by means of an eddy-relaxation source term that provides a combined model for forcing and dissipation. The relaxation parameter defines the amount of correlation of the subfilter forcing with resolved quantities. Its proper calibration is achieved using decaying homogeneous isotropic turbulence. Furthermore, characteristics of the backscatter forcing are analyzed from synthetic turbulence data. The first jet-wing interaction problem studied is based on a generic static jet interacting with a non-inclined rectangular wing. The second problem deals with a dual-stream nozzle installed at a high-lift wing with deployed flap and slat in wind tunnel flow under approach conditions. For both problems installation noise from the airframe yields higher peak levels than the jet-noise contribution alone. For the first problem, relative to the corresponding jet spectrum a low-frequency narrow-band contribution is observed that can be attributed to coherent jet structures interacting with the airfoil trailing edge. Very good agreement with measured spectra is obtained. For the second problem a broadband airframe installation contribution to the overall spectrum is predicted with peak frequency above the jet contribution.

I.   Introduction

Jet-flap installation noise arising from the interaction of the jet with the high-lift wing has become the concern for modern transport aircraft with ultra high bypass ratio jet engines mounted in closest possible proximity to the wing.

This work presents results obtained with partly scale resolving simulation for two different jet-flap interaction noise problems. The simulation approach utilizes coarse meshes, with the mesh resolution inferred from an estimate of the scales necessary to capture the essential aeroacoustics sound generation and radiation characteristics over the interesting frequency range. Similar to very large-eddy simulation (VLES),[1] the very large scales of turbulent fluctuations resolved on the mesh are directly calculated and the dissipation of the non-resolved scales is accounted for by a vorticity based Smagorinsky-like subgrid scale stress model.[2]

In addition, stochastic forcing in space and time is applied in the CAA simulation utilizing the Fast Random Particle-Mesh method (FRPM)[3–5] to model turbulent backscatter, i.e. 'the effect of random subgrid-scale (SGS) motion on the resolved (filtered) scales of turbulent motion', referring to Schumann.[6]

---

[*]Senior Scientist, Senior Member AIAA, corresponding author: roland.ewert@dlr.de.
[†]Research Scientist, Member AIAA.
[‡]Research Scientist, Member AIAA.

In general, the contribution of backscatter to the turbulent production in the well resolved scales grows continuously with reduced mesh resolution.[7] As was demonstrated for channel flow simulations,[8] stochastic forcing has the potential to significantly lower LES resolution requirements. Otherwise, chances are that the missing backscatter contribution, i.e. a lack of forcing of the resolved scales by non-resolved scales, poses limits on the mesh coarseness achievable without degradation of the resolved large scales physics.

Two different jet-wing installation problems are presented in this work. First, a generic jet installation noise problem studied in the framework of the EU project JERONIMO is considered using a single stream jet at $M_j = 0.6$ without background flow in combination with a rectangular unswept wing.

The second problem deals with a dual-stream nozzle installed at a high-lift wing with deployed flap and slat (F16 geometry) with wind tunnel co-flow under approach conditions, studied in the framework of the German national project POWER25, refer to Fig. 1.
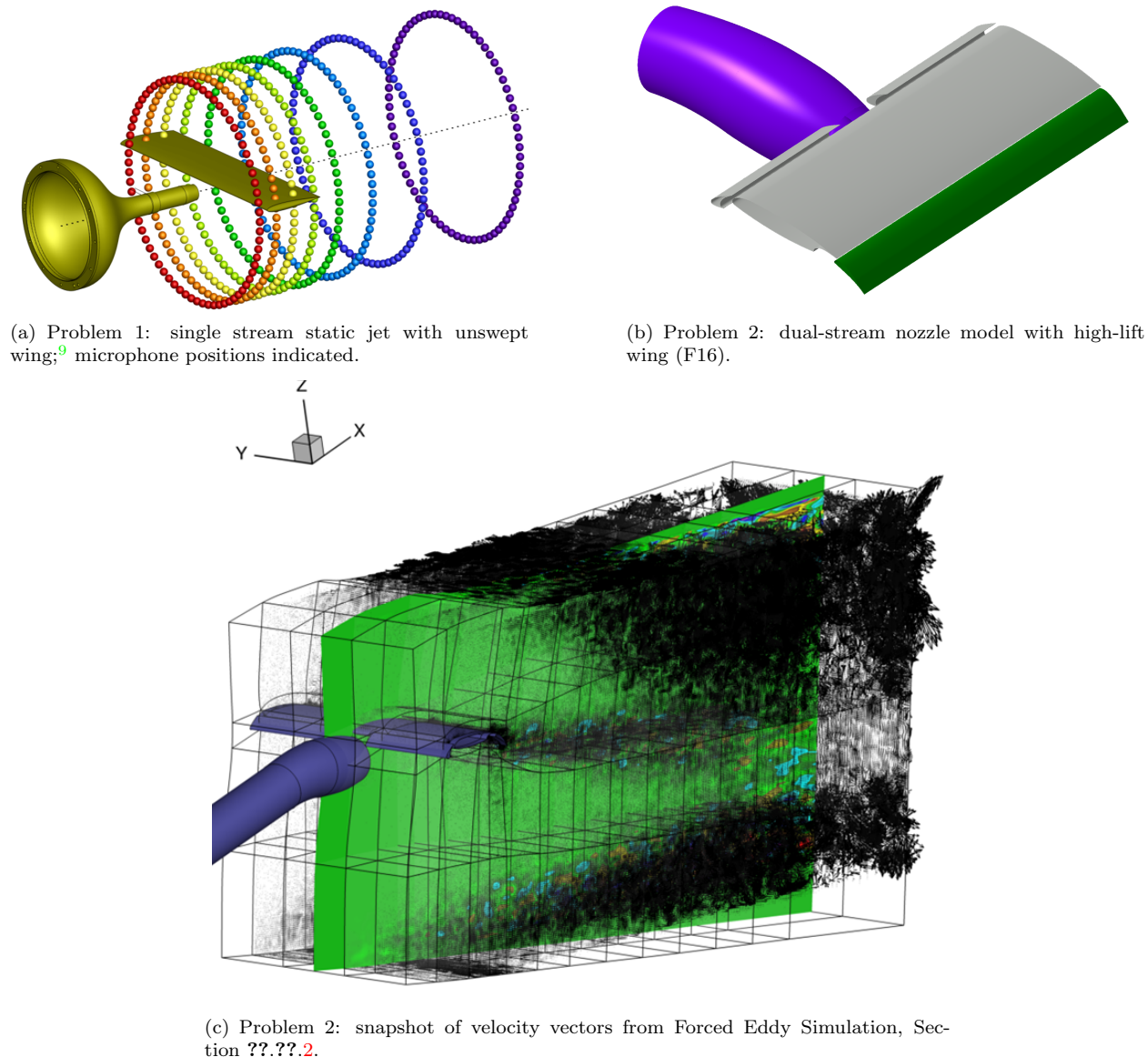

(a) Problem 1: single stream static jet with unswept wing;[9] microphone positions indicated.

(b) Problem 2: dual-stream nozzle model with high-lift wing (F16).

(c) Problem 2: snapshot of velocity vectors from Forced Eddy Simulation, Section ??.??.2.

Figure 1. Simulation problems.

Section II discusses the rationale of applying explicit backscatter forcing. Section III gives an overview on the numerical method applied in this work. Section IV discusses the calibration of the backscatter model. Results of the application test cases are presented in Section V. A summary with conclusions is given in Section VI.

American Institute of Aeronautics and Astronautics

II. Backscatter Rationale

A. Forced Incompressible Navier-Stokes Equations

In the next section the simulation method applied in this work will be outlined for the incompressible Navier-Stokes equations to clarify its basic general principle and to discuss the simulation strategy and its rationale.

The incompressible Navier-Stokes equations are given by (e.g. refer to Stewart,[10] Chp. 10)

$$\frac{\partial v_i}{\partial t} + \frac{\partial}{\partial x_j}\left(v_i v_j\right) + \frac{1}{\rho}\frac{\partial p}{\partial x_i} - \nu\frac{\partial^2 v_i}{\partial x_j^2} = 0, \quad \frac{\partial v_i}{\partial x_i} = 0, \tag{1}$$

where v_i indicates flow velocity, ρ density, p pressure and ν molecular viscosity. As being written in tensor notation (implying usage of Einstein's tensor notation for terms of equal indices), the momentum equation provides a covariant tensor equation for the velocity vector that is valid for any arbitrary inertial frame of reference moving at constant velocity, i.e. the momentum equation is Galilean invariant. Volume averaging of the first momentum equation yields

$$\frac{\partial \overline{v_i}}{\partial t} + \frac{\partial}{\partial x_j}\overline{v_i v_j} + \frac{1}{\rho}\frac{\partial \overline{p}}{\partial x_i} - \nu\frac{\partial^2 \overline{v_i}}{\partial x_j^2} = 0. \tag{2}$$

Here, volume averaging is indicated by the overbar. Furthermore, it is assumed that the applied volume averaging commutes with differentiation, i.e. $\overline{\frac{\partial \varphi}{\partial x}} = \frac{\partial \overline{\varphi}}{\partial x}$, and satisfies $\overline{\varphi_1 + \varphi_2} = \overline{\varphi_1} + \overline{\varphi_2}$. Assuming a sharp spectral cut-off filter, furthermore $\overline{\overline{\varphi}} = \overline{\varphi}$ holds.

The volume averaging procedure implies a sub-filter contribution, defined for velocity by $v_i' := v_i - \overline{v_i}$.

Based on this decomposition and using the previous filter relations, the filtered non-linear term can be rewritten as

$$\overline{v_i v_j} = \underbrace{\overline{\overline{v_i}\,\overline{v_j}}}_{I} + \underbrace{\overline{\overline{v_i}v_j'}}_{II} + \underbrace{\overline{v_i'\overline{v_j}} + \overline{v_i'v_j'}}_{III}. \tag{3}$$

For a sharp spectral filter, terms $(II) + (III)$ correspond to the well known sub-filter cross- and Reynolds-stresses[11] and term (I) is contributor to the Leonard stress term.[11] This decomposition allows to further rewrite Eq. (2) as

$$\frac{\partial \widetilde{v_i}}{\partial t} + \frac{\partial}{\partial x_j}\widetilde{v_i}\widetilde{v_j} + \frac{1}{\rho}\frac{\partial \widetilde{p}}{\partial x_i} - \nu\frac{\partial^2 \widetilde{v_i}}{\partial x_j^2} = \widetilde{f}_i(\widetilde{v_i}, v_i'), \tag{4}$$

Here the tilde is introduced to indicate that the resolved quantities are volume averaged quantities, i.e., $\widetilde{v_i} = \overline{v_i}$, however there is no explicit volume averaging needed to obtain them, rather Eq. (4) represents the governing equation of resolved velocity. Note, the overbar indicates explicit volume averaging. The forcing

$$\widetilde{f}_i := -\overline{\frac{\partial}{\partial x_i}\left(\overline{v_i}v_j' + v_i'\overline{v_j} + v_i'v_j'\right)} \tag{5}$$

defines the sub-filter forcing. Although it is formulated in terms of sub-filter quantities, the explicit filtering operation restricts the forcing just to resolved scales (as indicated by the tilde symbol on top of the forcing term). It is easy to proof that for a sharp cut-off filter Eq. (4) conserves Galilean invariance[a].

B. Discussion of Volume Averaged Equation

Sharp spectral filtering involves a specific cut-off wave-number (length scale). The exact mathematical derivation of Eq. (4) implies that it is general valid for any filter length scale applied, provided the right-hand side subfilter forcing would be given. That is, applying a large filter width yields a coarse grained solution, nevertheless the resolved variables comprise the physical solution up to the level of resolution.

Qualitatively, one would expect an increasing contribution of the subfilter forcing with increasing filter width.[7] At a specific scale, however, the trend must reverse to provide a decreasing contribution as for an arbitrary large filter width the energy of the resolved quantities tends to zero, which implies zero forcing.

---

[a]E.g., refer to Pope,[12] exercise 13.19.

The volume averaged governing equations are often used to motivate the rationale behind large eddy simulation (LES). Other than implied by Eq. (4), in scale resolving simulation such as LES or Detached Eddy Simulation (DES), it is observable that a sufficient fine mesh is needed to properly capture turbulent flow. Above a certain mesh resolution threshold the simulation quality deteriorates significantly and/or turbulent production is not maintained anymore.

As pointed out by O'Neill,[13] the majority of SGS parameterizations used in LES modeling are purely dissipative, implying that they seek to represent the net energy transfer rather than the forward and backward scatter separately, i.e.,

$$\widetilde{f}_i(\overline{\boldsymbol{v}}, \boldsymbol{v}') \simeq \widetilde{f}_i^D(\overline{\boldsymbol{v}}), \tag{6}$$

where $\widetilde{f}_i^D(\overline{\boldsymbol{v}})$ denotes a dissipative model relying on resolved quantities.

A subfilter model entirely defined by resolved quantities implies correlation 1.0 between subfilter forcing and resolved scales. However, for DNS simulation a typical correlation between residual stresses and strain rates between 0.16 and 0.5 is reported.[6] Correlation less than one imply that the right-hand side forcing term in Eq. (4) comprises also stochastic contributions that are uncorrelated to the resolved and provide a turbulent production in the resolved regime by non-resolved quantities. As pointed out by Westbury et al.,[14] the forward scatter (towards smaller scales) and backscatter (towards larger scales) of energy within a turbulent flow are often large and comparable in magnitude. Leslie and Quarini[15] found that the ratio of backscatter production to the net energy transfer rate can be greater than unity.

The amount of turbulent backscatter production, denoted hereafter as $\widehat{B}$, can be related to the turbulent dissipation rate $\mathcal{E}$ as the measure of the turnover of energy in a turbulent flow. In the literature, the backscatter production rate is estimated using the ansatz

$$\widehat{B} = c_B \mathcal{E} \times g_B\left(\frac{l_c}{L_f}\right), \tag{7}$$

where c_B is a backscatter constant and g_B is a function of mesh resolution l_c and turbulent length scale L_f which is of order $\mathcal{O}(1)$ in the inertial subrange, refer to the following discussion in the next section. This implies that backscatter remains important for all LES simulations with resolution below the Kolmogorov wave number scale. The backscatter constant is reported by Chasnov[16] and others[6,17,18] to be in the range

$$c_B = 0.4 \ldots 1.4. \tag{8}$$

A considerable amount of work has been been already published aiming to augment datum purely dissipative subgrid stress models with stochastic forcing,

$$\widetilde{f}_i \simeq \widetilde{f}_i^D + \widetilde{f}_i^F, \tag{9}$$

to model backscatter, e.g. refer to the work of Leith,[19] Schumann[6]), Mason & Thomson,[18] Marstorp et al.,[20] Weinbrecht & Mason,[17] and O'Neill et al.[13] in the framework of time-domain LES simulation.

For the solution of the Navier-Stokes equations in wave-number space, stochastic forcing has been studied e.g. in the framework of Renormalization Group Theory (RNG, refer to Yakhot & Orszag,[21,22] Smith & Woodruff,[23] Zhou,[24] Lesieur[25]) and the Eddy Damped Quasi Normal Markovian (EDQNM) model (Orzag,[26] Lesieur[25]) to maintain non-decaying homogeneous isotropic turbulence in the incompressible forced Navier-Stokes equations.

One could conjecture that the resolution limits observed in datum scale resolving simulation is related to a missing active forcing contribution that sustains turbulence even on coarse meshes where turbulence producing scales otherwise are filtered away by a filter too coarse.

Active volume forcing may help also to overcome the gray area problem, as turbulence is continuously forced over the simulation domain, i.e. no sudden transition from steady to scale resolving areas is present.

So far, backscatter simulations have been conducted for generic problems involving simple geometries. Active backscatter simulations might benefit from the development of stochastic methods developed in the framework of CAA to model turbulent sound sources of inhomogeneous and complex flows. They are useful to extend the range of applicability of stochastic backscatter models towards more complex geometrical problems of direct technical relevance.

As outlined in the subsequent sections, in this work the entire turbulent forcing function $\widetilde{f}_i$ is modeled by means of a relaxation source term (eddy-relaxation model[27]) that provides forcing and dissipation in a combined model and not as separate features.

American Institute of Aeronautics and Astronautics

III. Simulation Method

To capture subsonic sound generation, the sketched incompressible method it is extended to compressible flow following the simulation approach as being used by Tam & Kurbatski[28–30] for Direct Numerical Simulation (DNS) simulation of subsonic cold-flow sound problems. Refer also to the discussion of this approach in Ref.[27] The subfilter forcing terms of the momentum equation are used as discussed for the incompressible case. Those of the energy are omitted, restricting the approach to cold subsonic problems.

The equations are solved in perturbation form[27] using a solution of the time-averaged Reynolds Averaged Navier-Stokes equation as a background flow. The perturbation form does not change the forcing term as discussed for the complete incompressible equations.

The present equation serves as a starting form. The extension to include backscatter forcing also in the energy equation that removes the datum subsonic cold-flow restrictions will be tackled in some ongoing work.

The simulations are carried out with the Computational Aeroacoustics (CAA) code PIANO[31] of DLR. The Navier-Stokes equations are solved in disturbance form over a time-averaged background flow with non-linear disturbance equations (NLDE) as prescribed in Ref.,[27] with the stationary background flow obtained from precursor Reynolds Averaged Navier-Stokes (RANS) simulation. PIANO is a parallelized structured multi-block code utilizing the DRP scheme proposed by Tam & Webb.[32] High wave-number spurious waves are removed optional either using artificial damping[32] or 6th order spatial filtering. Time integration is performed with an explicit 4th order Runge-Kutta scheme. At up- and downstream boundaries a sponge zone is applied to damp out turbulent fluctuations. At all other boundaries radiation conditions[32] are applied.

A. Relaxation model for subfilter forcing

The entire subfilter forcing is modeled as a relaxation source term on the right-hand side of the momentum equation utilizing the eddy-relaxation model[27] in the form

$$\widetilde{\boldsymbol{f}} = -\boldsymbol{\nabla} \times \left[\sigma \left(\widetilde{\boldsymbol{\Omega}}' - \widetilde{\boldsymbol{\Omega}}^{ref} \right) \right] = \underbrace{- \boldsymbol{\nabla} \times \left(\sigma \widetilde{\boldsymbol{\Omega}}' \right)}_{=: \boldsymbol{f}^D} + \underbrace{\boldsymbol{\nabla} \times \left(\sigma \widetilde{\boldsymbol{\Omega}}^{ref} \right)}_{=: \boldsymbol{f}^F}, \tag{10}$$

where the resolved fluctuating vorticity is indicated by

$$\widetilde{\boldsymbol{\Omega}}' = \boldsymbol{\nabla} \times \widetilde{\boldsymbol{v}}', \quad \text{or} \quad \Omega_i' = -\epsilon_{ijk} \frac{\partial v_k'}{\partial x_j}, \tag{11}$$

and $\widetilde{\boldsymbol{\Omega}}^{ref}$ denotes a a fluctuating vorticity forcing vector, which is generated with the Fast Random Particle Mesh (FRPM) method,[3–5] typically applied over almost the entire computational domain, refer to Fig. 2. The stochastic realization generates spatially variable fluctuations based on locally prescribed convection velocity, turbulence decay with specific local time scale, local length scale, and prescribed variance. The time scale and the variance of the resolved vorticity fluctuations are derived from RANS one-point statistics. The proper calibration is discussed in detail in Section IV.

In the relaxation model the parameter σ specifies how close target and actual solution are coupled. To be precise, the correlation between resolved and forcing (target) vorticity is

$$\frac{\overline{\Omega_i' \Omega_i^{ref}}}{\sqrt{\overline{(\Omega_i')^2}} \sqrt{\overline{\left(\Omega_i^{ref} \right)^2}}} \rightarrow \begin{cases} 0 & \text{for} \quad \sigma \rightarrow 0 \\ 1 & \text{for} \quad \sigma \rightarrow \infty \end{cases} \tag{12}$$

1. Deterministic Mode

The size of the relaxation parameter σ defines the mode of operation in the simulation. A high value of the relaxation parameter σ enforces close coupling of the resolved vorticity fluctuations to the forcing vorticity, i.e. the vorticity fluctuations are entirely prescribed by the stochastic model. This simulation mode is hereafter referred to as 'Deterministic Mode'. Since the relaxation source term is formulated as the curl of a forcing function, fluctuations of the acoustic particle velocity are not modified by the source term, i.e. acoustic propagation is not affected and the source region is transparent for acoustic waves, refer to the discussion and results in Ref.[27]

2. Forced Eddy Simulation

Small values of σ in conjunction with non-linear equations enable the direct resolution of turbulence dynamics as being triggered by production mechanisms resolved on the CAA mesh. By replacing σ by a subfilter eddy viscosity ν_R, term $\boldsymbol{f}^D$ corresponds to the fluctuating part of the subgrid scale force 'Model 3' studied by Dantinne et al. for Large Eddy Simulation (LES),[2] i.e.,

$$f_i^D \to -\epsilon_{ijk}\frac{\partial}{\partial x_j}\left(\nu_R\widetilde{\Omega}_k'\right). \tag{13}$$

The stochastic forcing is limited in the highest realized wave-number, i.e. restricted to scales larger than a cut-off length scale l_c derived from the resolution of the numerical scheme as a multiple of the mesh resolution Δ, so that the forcing is not present for smaller scales below l_c. Hence, for small-scale wave-numbers $f_i^F \to 0$ and the entire eddy relaxation term realizes a subfilter-stress model that effectively provides the dissipation of energy at small scales. The eddy relaxation term has been shown to provide an all-pass characteristic with very steep cut-off up to the cut-off length scale l_c.[27]

Hence, using a subfilter eddy viscosity related to the mesh scale l_c in conjunction with an adequate forcing, one could assume that this as a meaningful ansatz for an active backscatter model. However, this conjecture has to be substantiated further.

The detailed derivation of the subfilter eddy viscosity will be subject of Section IV. The discussion will show that the relaxation model of the complete subfilter forcing indeed provides a consistent backscatter model. The calibration procedure that defines the residual eddy viscosity as the effective relaxation parameter could be understood as a way to define the level of correlation of the entire subfilter forcing term with resolved quantities.

For a fine mesh a typical subfilter eddy viscosity tends to zero, i.e. $\sigma = \nu_R \to 0$ (all fluctuations resolved) and the simulation procedure realizes a direct noise computation (DNC) based on the NLDE as governing equations. For coarser grids the derived ν_R scaling provides a monotonic growth with increasing mesh spacing towards a Deterministic Modes simulation. However, for very coarse meshes the subfilter scaling reverses and provides $\nu_R \to 0$ for $l_c \to \infty$, refer to the discussion in Section II.

B. Stochastic Forcing with FRPM

The 'Random Particle-Mesh Method' (RPM) was introduced in 2005.[33] FRPM was proposed in 2007[3] as an improved numerical version with further increased efficiency. The main building blocks of FRPM consists of the following two elements:

1. Creation of a solenoidal (divergence free) field of fluctuations by superposition of model vortices of random strength and spatial shape (blob) function derived from Gaussian distribution; the vortices advect in a prescribed non-uniform mean-flow field.

2. Efficient numerical realization of the superposition of vortices via random particles and efficient recursive 1-D Gaussian filters applied on an auxiliary FRPM mesh (source patch).

Forcing fluctuations are realized by the superposition of P random particles,

$$f_i^F = \epsilon_{ijk}\frac{\partial}{\partial x_j}\sum_{p=1}^{P}G(\boldsymbol{x} - \boldsymbol{x}_p, l_c)\widehat{A}(\boldsymbol{x}_p)\,r_{pk}^n. \tag{14}$$

Here, f_i^F is the i-th component of the forcing at discrete time level n (dependence on n not explicitly indicated). The resulting velocity field is divergence free (solenoidal). The summation with index p runs over all random particles. The random particles are represented by their positions $\boldsymbol{x}_p$ and carry 3 Gaussian random variables r_{pk}^n per particle. Furthermore, p is the particle number, and k indicates the random variables. Their random variates are generated from an Ornstein-Uhlenbeck process involving a time scale τ_B, refer to the discussion in Ref.[34]

The particles are advected in a mean-flow, i.e. $\dot{\boldsymbol{x}}_p = \boldsymbol{v}_0$. The particle seeding and distribution is realized so that a constant particle density is obtained and maintained throughout each simulation.

The shape function $G\left(\boldsymbol{x} - \boldsymbol{x}', l_c\right)$ is a Gaussian distribution with standard deviation proportional to the mesh length scale l_c. The function $\widehat{A}$ specifies the actual local variance realized by the fluctuations. It is
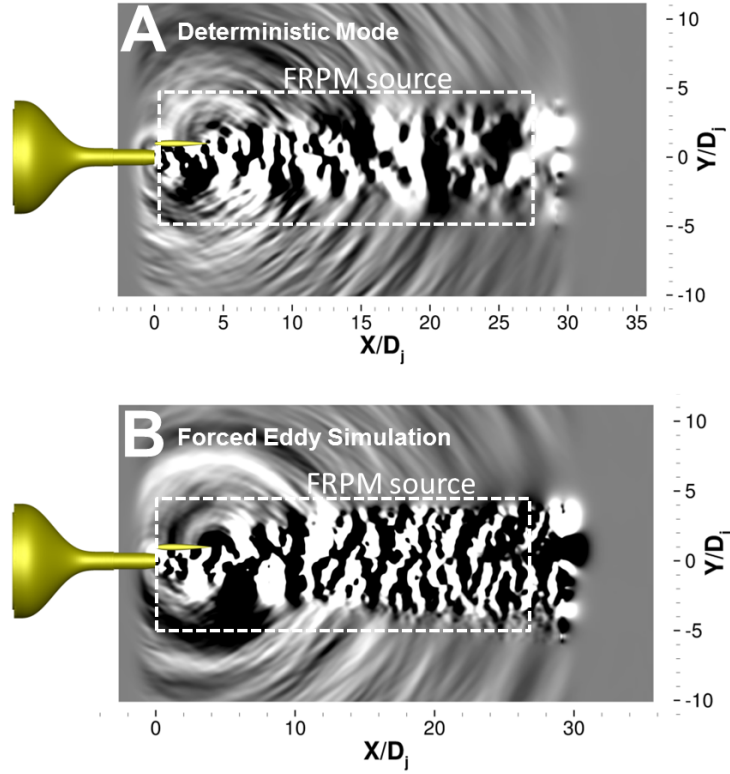
Figure 2. Pressure fluctuations in an intersection plane normal to the spanwise direction through the jet axis; A, Deterministic Mode simulation; B, Forced Eddy Simulation; the area where the forcing is applied is indicated with a dashed box.

$\widehat{A} = \sqrt{2\widehat{Q}/3\pi l_c}$. More details about the scaling can be found in Refs. [4,5]. In this way an energy spectrum of Gaussian shape and integral length scale l_c is realized.

For the numerical evaluation of Eq. (14) a direct simple computation of the shape function in the particle surroundings at $\boldsymbol{x}_p$ is avoided due to its numerical inefficiency. Rather, the random variates of each particle are projected via trilinear interpolation from the particle to an auxiliary background mesh (denoted as 'FRPM patch') that defines the resolved source area. The Gaussian is evaluated on the source patch via successive application of 1-D Gaussian filtering in each coordinate direction.[5] The typical speed-up for the evaluation of Eq. (14) yields 2 orders of magnitude compared to simple evaluation.

Furthermore, Gaussian filtering can be realized with optimized signal processing algorithms, e.g. those proposed by Young & van Vliet[35] (constant length scale) or that of Purser[36–38] (variable length scale). Application of the Young & van Vliet recursive Gaussian filter to the previous example yields a further speed up reaching a three orders of magnitude saving in computational time compared to simple evaluation of the sum.

The forcing-spectrum function $F(\kappa)$, $\widehat{F} := \left\langle \left(f_i^F\right)^2 \right\rangle = 2\int F(\kappa)\mathrm{d}\kappa$ created by the method reads

$$F(\kappa) = \frac{4l^5}{3\pi^3}\widehat{F}\kappa^4 \exp\left(-\frac{\kappa^2 l_c^2}{\pi}\right). \tag{15}$$

The scaling of $\widehat{F}$ and $\widehat{Q}$ will be discussed in the calibration section of this paper.

Hence, using FRPM to directly model fluctuating vorticity the major backscatter features as discussed in the literature are realized:

- backscatter-spectrum with k^4-slope for small wave-numbers (Leith 1990,[19] Schumann 1995[6])

- divergence-free (solenoidal) forcing (Leith 1990,[19] Mason & Thomson 1992,[18] Schumann 1995[6])

- spatial correlation length scale of forcing defined by local mesh resolution (Leith 1990,[19] Schumann 1995[6])

- forcing defined in a Lagrangian frame (Marstorp et al. 2007,[20] Schumann 1995[6])

Furthermore, the present forcing realizes a finite turbulent decay time-scale, which however, in the datum simulations is based on the turbulent time scale and not on the eddy turnover time used by Schumann[6] and Marstorp et al.,[20] and a spatially distributed forcing variance.

As pointed out by Weinbrecht & Mason, for a spatially variable backscatter variance, the curl operator applied to a stochastic vector potential creates a contribution proportional to the gradient of the backscatter variance. As found by Mason & Thomson, smoothing of the backscatter forcing variance with a 1 : 2 : 1 filter is recommended. The FRPM method allows to apply the amplitude scaling $\hat{A}$ before or after application of the Gaussian filtering, i.e. essentially realizing $\hat{A}(\boldsymbol{x})$ or $\hat{A}(\boldsymbol{x}_p)$, respectively. The latter option is applied in this work and effectively yields a smoothing of the forcing variance with a Gaussian related to the resolved mesh length scale l_c.

To comply with the forcing characteristics, the spatially variable subfilter eddy viscosity ν_R is also filtered before usage with a Gaussian filter of length scale l_c. This procedure is also indicated considering the subfilter forcing Eq. (5), which must comprise subfilter features on the level of the filter scale applied.

IV. Backscatter Model Calibration

A. DHIT Calibration of Stochastic Backscatter Forcing

1. Problem description

The calibration of the backscatter model is conducted in a two-step approach based on DNS reference data of Wray[39] for Decaying Homogeneous Isotropic Turbulence (DHIT). The initial turbulence spectrum is specified by an initial turbulence kinetic energy, dissipation rate, and spectrum peak level, respectively given by[40]

$$k_t = 0.95 m^2/s^2, \quad \mathcal{E} = 1.56 m^2/s^3, \quad \kappa_{max} = 4.0. \tag{16}$$

An initial turbulent length scale

$$L_f = c_l \frac{k_t^{3/2}}{\mathcal{E}} \tag{17}$$

infers from turbulence kinetic energy and dissipation rate. For a von Kármán spectrum it is $c_l \approx 0.54$, which yields $L_f \approx 0.3205$m.

The goal is to capture a proper decay just up to a cut-off wave-number related to the proper resolution limit of the numerical scheme applied. For example, for the DRP scheme of Tam & Webb[32] used for the present study, a meaningful resolution limit is given by a cut-off wave-number κ_c related to 5PPW (Points-Per-Wave-length) mesh resolution, i.e. clearly above the mesh Nyquist wave-number κ_n of 2PPW. A corresponding ratio $\kappa_n/\kappa_c = 2.5$ is considered for the present calibration.

The typical decay behavior involves a decay of the spectrum peak amplitude, accompanied by a successive shift of the spectrum peak wave number to lower wave-numbers, refer to Fig. 4. Thick solid lines therein indicate the DNS reference solution.

Typically, the turbulent kinetic energy that results from the integral of the turbulence spectrum over wave-number exhibits a decay at power law t^{-n}, $n \simeq 1.15 - 1.45$, refer to Pope,[12] Chp. 10.4.

The data is non-dimensionalized based on the speed of sound c_0 as reference velocity, a reference length scale $L_{ref} = 1$m, and a reference time scale $T_{ref} = L_{ref}/c_0$. Simulations are carried out on a cube with non-dimensional edge length 2π. Hence, the non-dimensional mesh resolution is given by $\Delta = 2\pi/N$. From the mesh spacing the non-dimensional Nyquist and cut-off wave-numbers deduce as $\kappa_n = \pi/\Delta$.

2. Calibration procedure

The decay simulations are conducted on three different meshes with resolutions $N = 32^3$, 64^3, and 128^3 grid points, respectively, Fig. 6. Hence, cut-off wave-numbers are given by $\kappa_c = \kappa_n/2.5 = 6.4$, 12.8, and 25.6, respectively for each mesh.

In a first calibration step, an eddy-viscosity is defined applying no forcing. Figs. 4 and 5 show examples from the calibration procedure based on 32^3 and 64^3 resolution, respectively. On the left, Figs. 4(a) and 4(b),
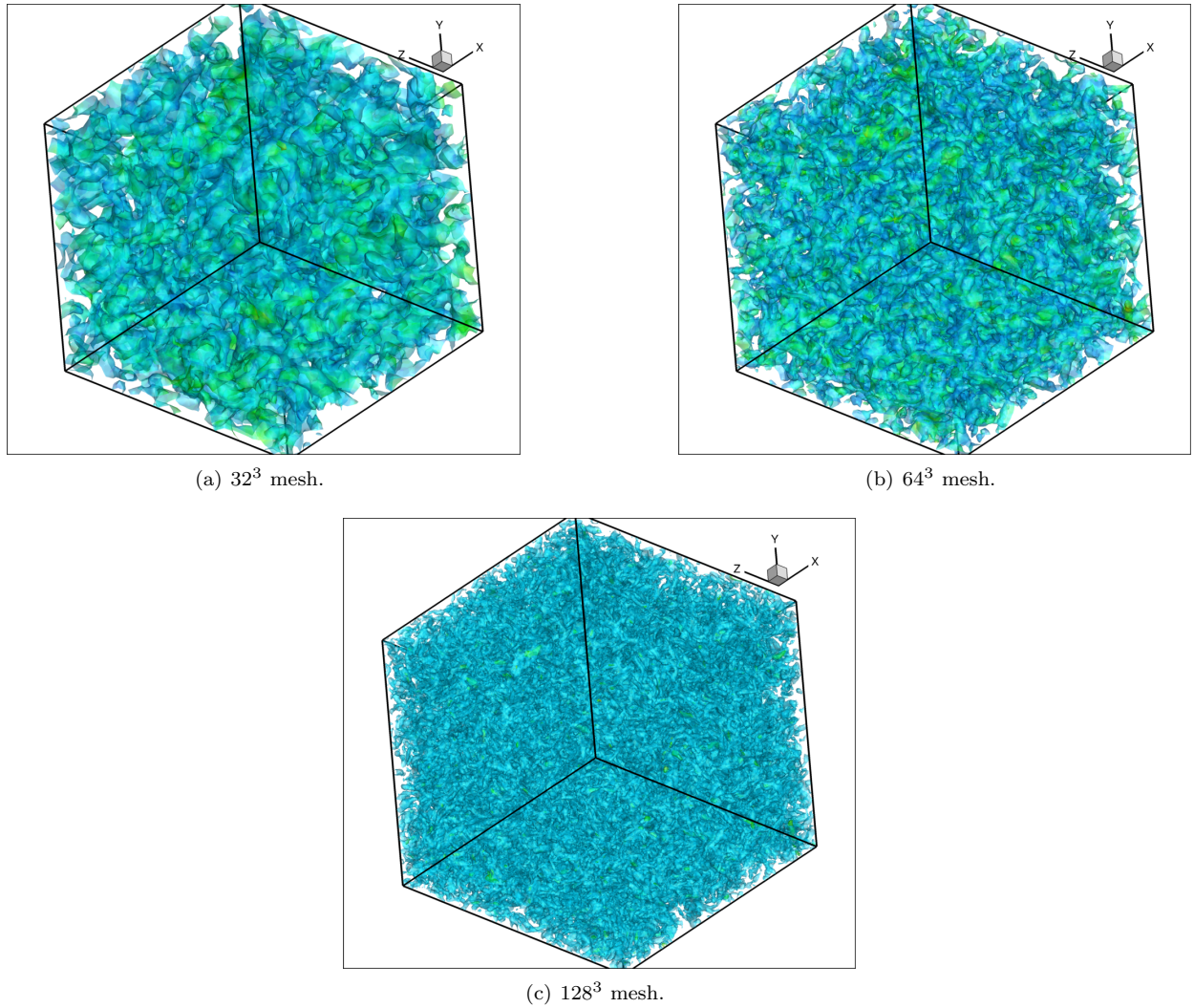
American Institute of Aeronautics and Astronautics

(a) 32^3 mesh.

(b) 64^3 mesh.

(c) 128^3 mesh.

Figure 3. DHIT test solutions for different mesh resolutions; iso-contours of x-, y-, and z-vorticity shown; colormap related to vorticity magnitude.

only ASD regularization for removal of spurious wave-modes is applied with damping constant $\sigma = 0.005$. It is visible that an energy pile-up to higher frequencies results. However, the decay at lower wave-number is captured, indicating transport of energy from small to large wave-numbers by the non-linear terms. Figs. 4(b) and 5(b)show results using a best calibrated eddy-viscosity in the model Eq. (10) without forcing. Note, results are shown adopting the non-dimensional time levels used by Wray based on a reference velocity $\sqrt{k_t}$ instead of c_0.

With an appropriate eddy-viscosity, a decay can be adjusted that captures the proper shift and decay of the peak amplitude according to the DNS reference data. Furthermore, for wave-numbers below and in a regime above the spectral maximum, the simulation follows the DNS characteristics very well, e.g. no energy pile-up to higher wave-numbers is visible.

However, a typical behavior is observable, showing a successively earlier drop-off of the spectrum even below the intended mesh cut-off wave-number (indicated as a thick vertical line in the plots Fig. 4) with increasing time level, refer to the numerical solutions indicated by thin solid lines in the figures. Note, this spectral gap is attributed to the lack of backscatter turbulence production.

Indeed, the specific shape of the forcing spectrum with an κ^4 increase up to the intended cut-off wave-number–refer to the discussion in IV.B–supports an additional turbulence production in the spectral gap below the cut-off wave-number and thus would support enrichment of the spectrum up to the desired cut-off wave-number.
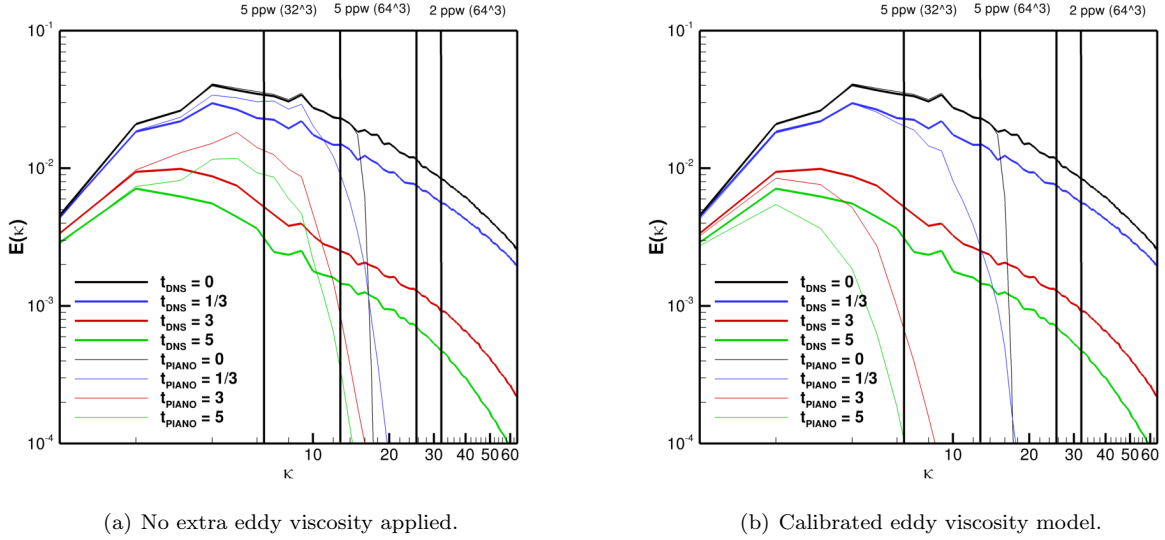
(a) No extra eddy viscosity applied.

(b) Calibrated eddy viscosity model.

Figure 4. DHIT test on 32^3 mesh.

(a) No extra eddy viscosity applied.
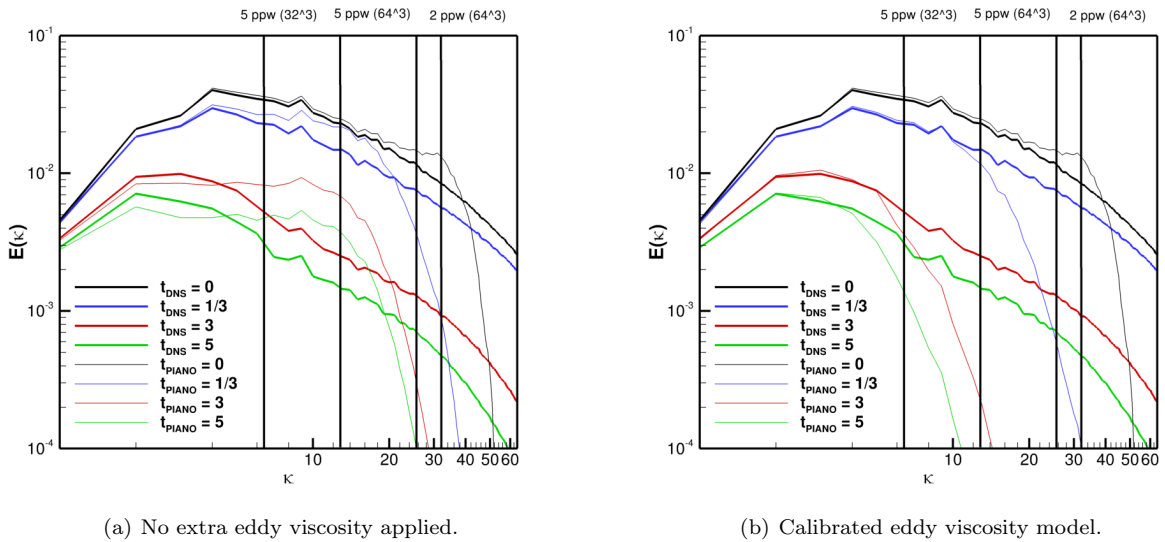
(b) Calibrated eddy viscosity model.

Figure 5. DHIT test on 64^3 mesh.

Therefore, in a second step after successful calibration of the residual stress model part, active forcing is applied to further extend the range of the resolved turbulence spectrum.

With forcing applied, the intended cut-off wave-number eventually results from the forcing cut-off, i.e. can be deliberately adjusted. The length scale of the Gaussian used for the datum forcing spectrum is fixed to a length scale $l_c = 2\pi\beta/\kappa_c$. The factor $\beta = 2/5$ (i.e. $l_c = 2\Delta$) accounts for the smooth roll-off of the Gaussian forcing spectrum. With the chosen value the intended cut-off around $\kappa_c/\kappa_n = 2.5$ is obtained.

3. Calibration of residual eddy viscosity

The previously sketched calibration procedure is conducted for all three meshes. The calibration involves three relevant physical parameters (i.e. k_t, ϵ, and l_c) and two physical units (m and s).

Consequently, on dimensional grounds the eddy viscosity must be given by a dimensional factor $\nu_t := c_u k_t^2/\mathcal{E}$ times a non dimensional scaling function of non-dimensional parameter l_c/L_f, with L_f as defined by

American Institute of Aeronautics and Astronautics

Eq. (17). As indicated, the dimensional factor corresponds to the RANS eddy viscosity ν_t using a parameter $c_\mu \approx 0.09$. Thus, the residual eddy viscosity must be given by the relationship

$$\nu_R = \nu_t \times g_\nu \left(\frac{l_c}{L_f} \right) \left[\frac{m^2}{s^4} \right]. \tag{18}$$

For the present calibration study, all spectra are located in the inertial sub range, so that a power law is assumed for the unknown scaling function.

For a spectrum with $-5/3$ roll-off, the exponent can be derived as $m = 4/3$, refer e.g. to the discussion in Pope,[12] Chp. 13.4. Thus, the residual eddy viscosity is assumed to be described by a scaling law

$$\nu_R = \beta_5 \nu_t \left(\frac{l_c}{L_f} \right)^m = \beta_6 \nu_t \left(\frac{\kappa_c}{\kappa_{max}} \right)^{-m}. \tag{19}$$

The second of the above expressions is suitable for the present calibrations where ratios κ_c/κ_{max} are given, refer to the previous discussion.

In an application using a steady RANS background flow to derive the residual stresses, the first expression would be more suitable since RANS provides values for L_f and ν_t, and l_c is the resolution related to the CAA mesh used.

The constant β_6 follows from the present calibration. According to the previously given parameters, the two calibrations constants are related via

$$\beta_5 = \beta_6 \left(\frac{5}{4\pi\beta_2} \right)^m. \tag{20}$$

The parameter β_2 defines the relationship between integral length scale and peak wave-number of the turbulent spectrum, $L_f = \beta_2 \cdot \kappa_{max}^{-1}$. For a von Kármán spectrum it is $\beta_2 = 1.339$[b]. Eventually, this yields $\beta_5 = 0.1983\beta_6$ for the parameter suitable for application with RANS background mean-flow data.

With the theoretical motivated exponent $m = 4/3$ a meaningful calibration could be achieved for different mesh resolutions, refer to the results shown in Fig. 3. The constant $\beta_6\nu_t$ are given in Tab. 1. From initial values Eq. (16) a dimensional initial turbulent viscosity infers as $\nu_t^* = 0.05207\text{m}^2/\text{s}$. Based on the values shown in Tab. 1 the constants infer as

$$\beta_6 = 0.961, \quad \text{and} \quad \beta_5 = 0.191. \tag{21}$$

4.   Calibration of stochastic forcing

Next the calibration of forcing term $\boldsymbol{f}^F$ in Eq. (10) is considered. A similar calibration procedure as discussed for the eddy viscosity before can be applied to fix the forcing variance

$$\hat{F} := \overline{\left(f_i^F \right)^2}. \tag{22}$$

The forcing in the eddy relaxation model Eq. (10) is obtained by taking the curl of a vector potential $\boldsymbol{q} := \nu_R \boldsymbol{\Omega}^{ref}$, i.e,.

$$\boldsymbol{f}^F = \boldsymbol{\nabla} \times \boldsymbol{q}, \quad \text{or} \quad f_i^F = \epsilon_{ijk} \frac{\partial q_k}{\partial x_j}.$$

The vector potential is defined by absorbing the eddy viscosity in the reference forcing vorticity. Effectively, it is the vector potential that is generated with FRPM based on mutually uncorrelated vector components. The final task therefore is the proper definition of the source variance

$$\widehat{Q} := \left\langle q_i^2 \right\rangle \tag{23}$$

---

[b]This implies for the Wray spectrum with $\kappa_{max} = 4.0$ a length scale $L_f = 0.33475$, i.e. a value slightly above the value as provided by Eq. (17). The difference might be attributed to uncertainties related to the derivation of k_t, $\mathcal{E}$ and differences between assumed and real shapes of the turbulence spectrum. However, the difference is less than 5%, i.e. perhaps of well bearable magnitude.
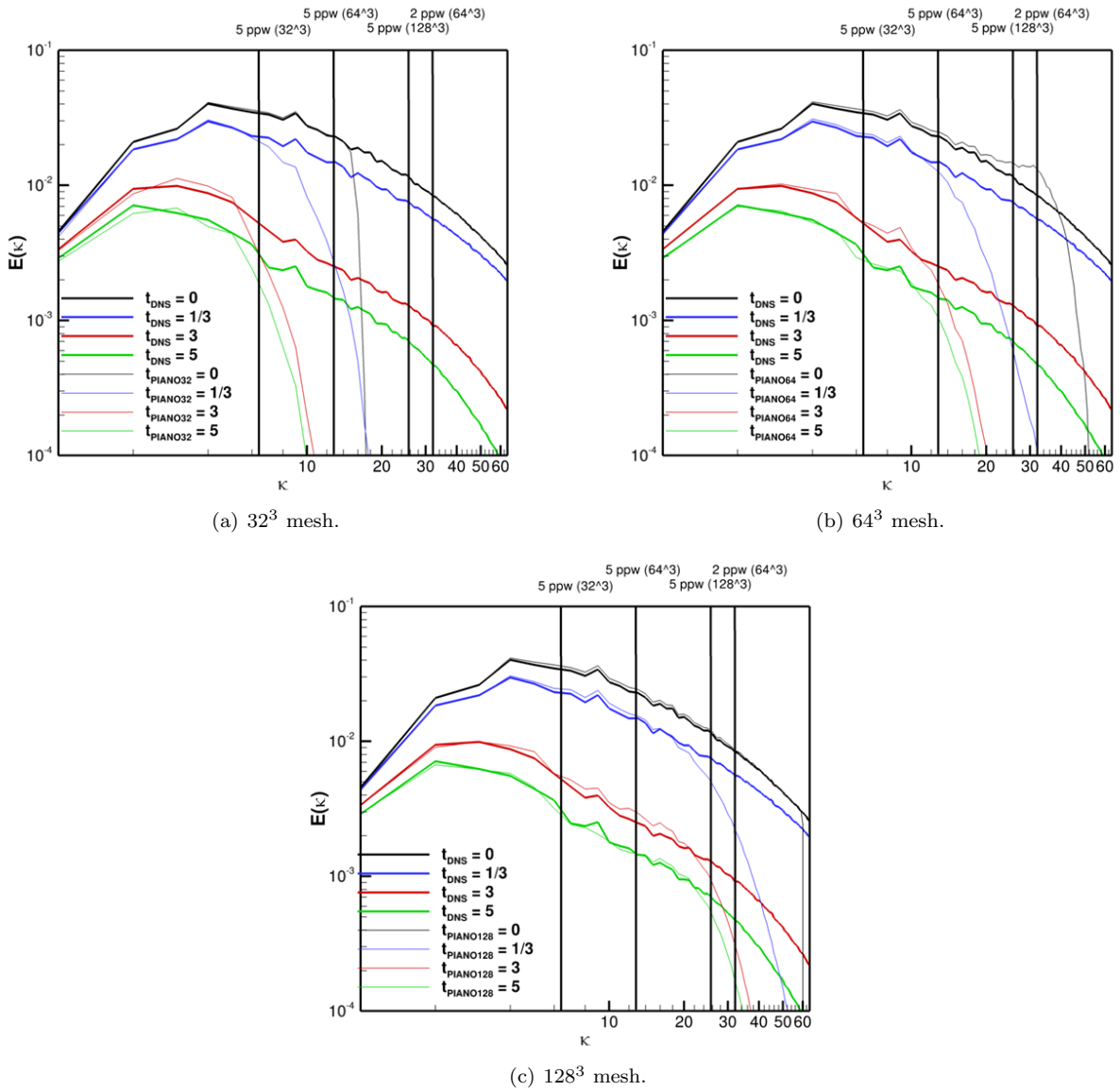
(a) 32^3 mesh.

(b) 64^3 mesh.

(c) 128^3 mesh.

Figure 6. DHIT simulation with stochastic forcing applied.

to accomplish a specific desired forcing variance $\widehat{F}$. From an independent calibration of the subfilter eddy viscosity ν_R and the source variance $\widehat{Q}$, an effective forcing vorticity variance derives via

$$\overline{\left(\Omega_i^{ref}\right)^2} = \frac{\widehat{Q}}{\nu_R^2}. \tag{24}$$

If the result agrees with the variance as expected for the reference vorticity, this provides a consistency check that substantiates the relaxation source model based backscatter ansatz Eq. (10) with common relaxation parameter ν_R.

The forcing variance can be expressed in terms of an appropriate dimensional scaling parameter times a non-dimensional scaling function of a non-dimensional characteristic number of all relevant variables involved, i.e. k_t, $\mathcal{E}$, and l_c. Consequently, the forcing variance reads

$$\widehat{F} = \frac{k_t^2}{L_f^2} \times g_F\left(\frac{l_c}{L_f}\right) \left[\frac{m^2}{s^4}\right], \tag{25}$$

where $g_F\left(\frac{l_c}{L_f}\right)$ is a scaling function yet to be specified. Remind, the length scale L_f, Eq. (17), is entirely

prescribed by the variables of the problem.

Similar to the residual eddy viscosity, in the inertial subrange it might be possible to assume the scaling function to be defined by a power law, thus

$$g_F\left(\frac{l_c}{L_f}\right) \stackrel{l_c \ll L_f}{\longrightarrow} \left(\frac{l_c}{L_f}\right)^{-r} \propto \kappa_c^r, \quad \text{and} \quad \widehat{F} \propto \kappa_c^r. \tag{26}$$

As an additional parameter of the stochastic forcing a decay time scale τ_B has to be specified, refer to the brief outline given in III.B for the Fast Random Particle-Mesh Method (FRPM) as applied in this work. To be precise, τ_B is the integral time scale related to the time-correlations $\langle q_i(\boldsymbol{x}, t) q_i(\boldsymbol{x}, t + \tau) \rangle$ of the source vector $\boldsymbol{q}(\boldsymbol{x}, t)$ in point $\boldsymbol{x}$. The source variance needed to obtain a specific forcing variance will be further outlined in the next paragraph.

The forcing has been tested with different fixed and variable time scales, i.e. using

$$\tau_B|_N = \tau_B|_{64} \left(\frac{\kappa_c|_{64}}{\kappa_c|_N}\right)^p, \tag{27}$$

where the additional sub script indicates the number of points involved, i.e. the time scale is calibrated for the case $N = 64$ and calibrated for the other mesh cases according to a cut-off wave-number based power law.

The time scale for the 64^3 mesh can be related to the turbulent time scale $k_t/\mathcal{E}$ via

$$\tau_B = c_\tau \frac{k_t}{\mathcal{E}}. \tag{28}$$

For $p = 0$ the time scale is independent from the mesh resolution, otherwise c_τ is a function of the mesh resolution.

Note, the forcing variance does not represent the actual backscatter variance that indicates the turbulence production achieved by the forcing term, i.e. the essential quantity accomplished by the forcing.

Rather, the turbulence production achieved by the forcing follows by recasting the momentum equation of resolved velocity fluctuations with applied forcing

$$\underbrace{\frac{\partial \widetilde{v}_i'}{\partial t} + \cdots}_{\mathcal{N}_i} = \widetilde{f}_i \tag{29}$$

into the corresponding governing equation for turbulent kinetic energy. The transport equation for the resolved turbulent kinetic energy $k_t = \langle (\widetilde{v}_i')^2 \rangle / 2$ derives by multiplying the momentum equation with $\widetilde{v}_i'$ and subsequent ensemble averaging of the resulting equation, i.e. from the term-by-term evaluation of $\langle \widetilde{v}_i' \mathcal{N}_i \rangle = \langle \widetilde{v}_i' \widetilde{f}_i \rangle$. Consequently, the backscatter variance follows from

$$\widehat{B} := \left\langle \widetilde{f}_i \widetilde{v}_i' \right\rangle. \tag{30}$$

As discussed by O'Neill et al.,[13] Weinbrecht & Mason,[17] Schuman,[6] and Mason & Thomson,[18] for a forcing correlated over time scale τ_B, the velocity built-up due to a fixed forcing over limited time τ_B can be estimated as $\delta \widetilde{v}_i' \propto \tau_B \widetilde{f}_i$. As all other velocity fluctuations are uncorrelated to the forcing, this yields $\left\langle \widetilde{f}_i \widetilde{v}_i' \right\rangle \simeq 1/2 \left\langle \widetilde{f}_i \delta \widetilde{v}_i' \right\rangle$. Upon inserting the estimate of $\delta \widetilde{v}_i'$ one arrives at $\left\langle \widetilde{f}_i \widetilde{v}_i' \right\rangle \propto \tau_B \left\langle \widetilde{f}_i \widetilde{f}_i \right\rangle$.

Test with different forcing parameters applied indicate that $\widehat{B} \propto \widehat{F} \tau_B$ is satisfied for a large range of time scales related to parameters $c_\tau < 1$. Thus, a good calibration could be found for different parameter values provided the product $\widehat{F} \tau_B$ remains invariant.

Based on power law parameters r and p and using $\widehat{B} \propto \widehat{F} \tau_B$, the backscatter variance infers to scale with an effective power law

$$\widehat{B} \propto \kappa_c^q, \quad \text{with} \quad q = r + p. \tag{31}$$

5. Source variance

The relationship between $\widehat{F}$ and $\widehat{Q}$ can be found following the discussion outlined in Ref.[4] to derive fluctuating velocity $\boldsymbol{v'}$ of variance $k_t = 1/2 \left\langle v_i^2 \right\rangle$ from the curl of a stochastic vector potential ψ_i of variance $\widehat{R} = 1/3 \left\langle \psi_i^2 \right\rangle$, $v_i = \epsilon_{ijk} \partial \psi_k / \partial x_i$ (adopting the notations of the paper). Making the replacements $1/3\widehat{Q} \to \widehat{R}$ and $1/2\widehat{F} \to k_t$ and using Eq. (21) of Ref.,[4] one arrives at

$$k_t = \frac{3\pi}{2l_s^2}\widehat{R} \quad \Rightarrow \quad \widehat{Q} = \frac{l_c^2}{\pi}\widehat{F}. \tag{32}$$

The quality l_s indicates the integral length scale realized for the velocity fluctuations. It is replaced by the cut-off length scale l_c here. Eq. (32) implies

$$\widehat{Q} \propto \kappa_c^m, \tag{33}$$

with $m = r - 2$.

6. Main results of forcing calibration

Results for the forcing calibration are summarized in Tabs. 1 and 2 using the residual eddy viscosity derived from the precursor tests without forcing based on a power law with $n = -4/3$. For Tab. 2 a constant non dimensional time scale $\tau_B = 45$ is used, which corresponds to a constant value of $c_\tau = 0.217$ and time scaling exponent $p = 0$. For Tab. 1 the same c_τ has been used for 64^3 resolution together with a scaling exponent $p = -2/3$. The source variance is chosen for all three case such that a best possible calibration is achieved. The effectively used initial source variance is varied over simulation time applying a decay law $\widehat{Q}\exp(-t/t_d)$ with $t_d = 150$ to take into account that the forcing contribution effectively also decays over time. Hence, the scaling power m is the numerical result of the calibration procedure.

From the powers n, m, and p the effective scaling of the forcing and backscatter variance are derived according to the previous discussion and as indicated in the tables.

As the main result, the backscatter power derives independent of the chosen time decay law as $q = 1.00 \ldots 1.33$. However, the choice of the time decay power has an influence on the forcing power r so that $q = r + p$ remain invariant, a results that confirms the theoretical relationship $\widehat{B} \propto \widehat{F}\tau_B$.

The evaluation of the subfilter forcing variance reported in the next paragraph reveals an inertial range scaling of the variance with power $r = 1.0$ for a Liepmann spectrum with -2 inertial decay and $r \simeq 1.33$ for $-5/3$ decay. This agrees with the scaling found in Tab. 2 and implies $r = 0.0$. That is, a time scale defined by Eq. (28) with a mesh independent scaling parameter c_τ. This time scale $\tau_B \propto L_f/\sqrt{k_t}$ differs from backscatter time scales inferred from an eddy turnover time scale assumed in other work as the relevant backscatter scale,[6] which implies $r \neq 0$.

However, in the application reported a RANS derived time scale ($r = 0$) has been used with $c_\tau = 0.02 \ldots 0.2$.

Taking the values from Tab. 2 and using the turbulence scales of the DHIT test case, the source variance calibration is deduced as

$$\hat{Q} = \gamma_1 k_t^2 \left(\frac{l_c}{L_f} \right) \tag{34}$$

with calibration constant

$$\gamma_1 = 0.0133[-].$$

This value is valid for $c_\tau = 0.217$.

7. General remark

The calibration procedure that defines the residual eddy viscosity as the effective relaxation parameter could be understood as a way to effectively define the level of correlation of the entire subfilter forcing term with resolved quantities.

Recall, a subfilter model entirely defined by resolved quantities implies correlation 1.0 between subfilter forcing and resolved scales. However, for DNS simulation a typical correlation between residual stresses and strain rates between 0.16 and 0.5 is reported.[6]

Furthermore, its worth to note that the forcing source variance $\widehat{Q} = \overline{q_i^2}$ as derived by the previously discussed calibration procedure in the inertial subrange regime is consistent with the variance that can be

Table 1. Calibration parameters obtained for different mesh resolutions, time scale depends of κ_c ($p = -2/3$).

mesh N^3	$\kappa_c|_N/\kappa_c|_{64}$ [-]	$10^5\nu_R$ [-]	$10^4\hat{Q}/\nu_R^2$ [-]	$10^{13}\hat{Q}$ [-]	τ_B [-]	n $\nu_R \propto \kappa_c^n$	m $\hat{Q} \propto \kappa_c^m$	p $\tau_B \propto \kappa_c^p$	$r = m+2$ $\hat{F} \propto \kappa_c^r$	$q = r+p$ $\hat{B} \propto \kappa_c^q$
32^3	0.5	7.87	1.12	6.94	71.43					
64^3	1	3.12	5.65	5.50	45.00	-1.33	-0.33	-0.67	1.67	1.00
						-1.33	0.00	-0.67	2.00	1.33
128^3	2	1.24	35.6	5.47	28.34					

Table 2. Calibration parameters for different mesh resolutions; time scale independent of κ_c ($p = 0$).

mesh N^3	$\kappa_c|_N/\kappa_c|_{64}$ [-]	$10^5\nu_R$ [-]	$10^4\hat{Q}/\nu_R^2$ [-]	$10^{13}\hat{Q}$ [-]	τ_B [-]	n $\nu_R \propto \kappa_c^n$	m $\hat{Q} \propto \kappa_c^m$	p $\tau_B \propto \kappa_c^p$	$r = m+2$ $\hat{F} \propto \kappa_c^r$	$q = r+p$ $\hat{B} \propto \kappa_c^q$
32^3	0.5	7.87	1.78	11.00	45.00					
64^3	1	3.12	5.65	5.50	45.00	-1.33	-1.00	0.00	1.00	1.00
						-1.33	-0.67	0.00	1.33	1.33
128^3	2	1.24	22.48	3.46	45.00					

directly derived from the relaxation source term $\boldsymbol{f}^F$ of Eq. (10). Comparison of the forcing term with the eddy relaxation term implies $f_i^F = \epsilon_{ijk}\partial\left(\nu_R\Omega_k^{ref}\right)/\partial x_j = \epsilon_{ijk}\partial q_k/\partial x_j$. Hence,

$$\widehat{Q} = \nu_R^2\zeta, \tag{35}$$

where $\zeta := \overline{\left(\Omega_i^{ref}\right)^2}$ defines the enstrophy. A physically motivated model for the resolved enstrophy was e.g. derived and discussed in Ref.,[34,41,42] yielding

$$\zeta = c_\zeta\frac{k_t}{l_c^2} = c_\zeta\frac{k_t}{L_f^2}\left(\frac{L_f}{l_c}\right)^2 \propto \frac{c_\zeta}{c_l^2}\frac{\mathcal{E}^2}{k_t^2}\kappa_c^2. \tag{36}$$

With the power-law scaling found from the calibration of the residual eddy viscosity, $\nu_R \propto k_t^2/\mathcal{E}\kappa_c^{-4/3}$, it follows

$$\widehat{Q} \propto \nu_R^2\zeta \propto k_t^2\kappa_c^{-2/3}. \tag{37}$$

This yields a forcing

$$\widehat{F} \propto \frac{k_t^2}{L_f^2}\kappa_c^{4/3}. \tag{38}$$

Both results for forcing and source variance are in agreement with the source scaling independently found from the calibration in the previous section.

On the contrary, from theoretical reasoning and evaluations with synthetic turbulence a scaling function is derived in this paper that for a homogeneous isotropic spectrum is also valid over the entire range of wave-numbers,

$$\widehat{Q} \propto k_t^2\left(\frac{l_c}{L_f}\right)^2 g_F\left(\frac{l_c}{L_f}\right). \tag{39}$$

Thus, using Eqs. (35) and (36) a model for ν_R can be derived for the entire wave-number range,

$$\nu_R = \sqrt{\frac{\widehat{Q}}{\zeta}} \propto \nu_t \underbrace{\left(\frac{l_c}{L_f}\right)^2\sqrt{g\left(\frac{l_c}{L_f}\right)}}_{g_\nu}. \tag{40}$$

American Institute of Aeronautics and Astronautics

This defines the scaling function g_ν, Eq. (18). The missing calibration constant can be found by matching the function in the asymptotic regime to the values found by calibration.

B. Backscatter Characteristics from Synthetic Turbulence
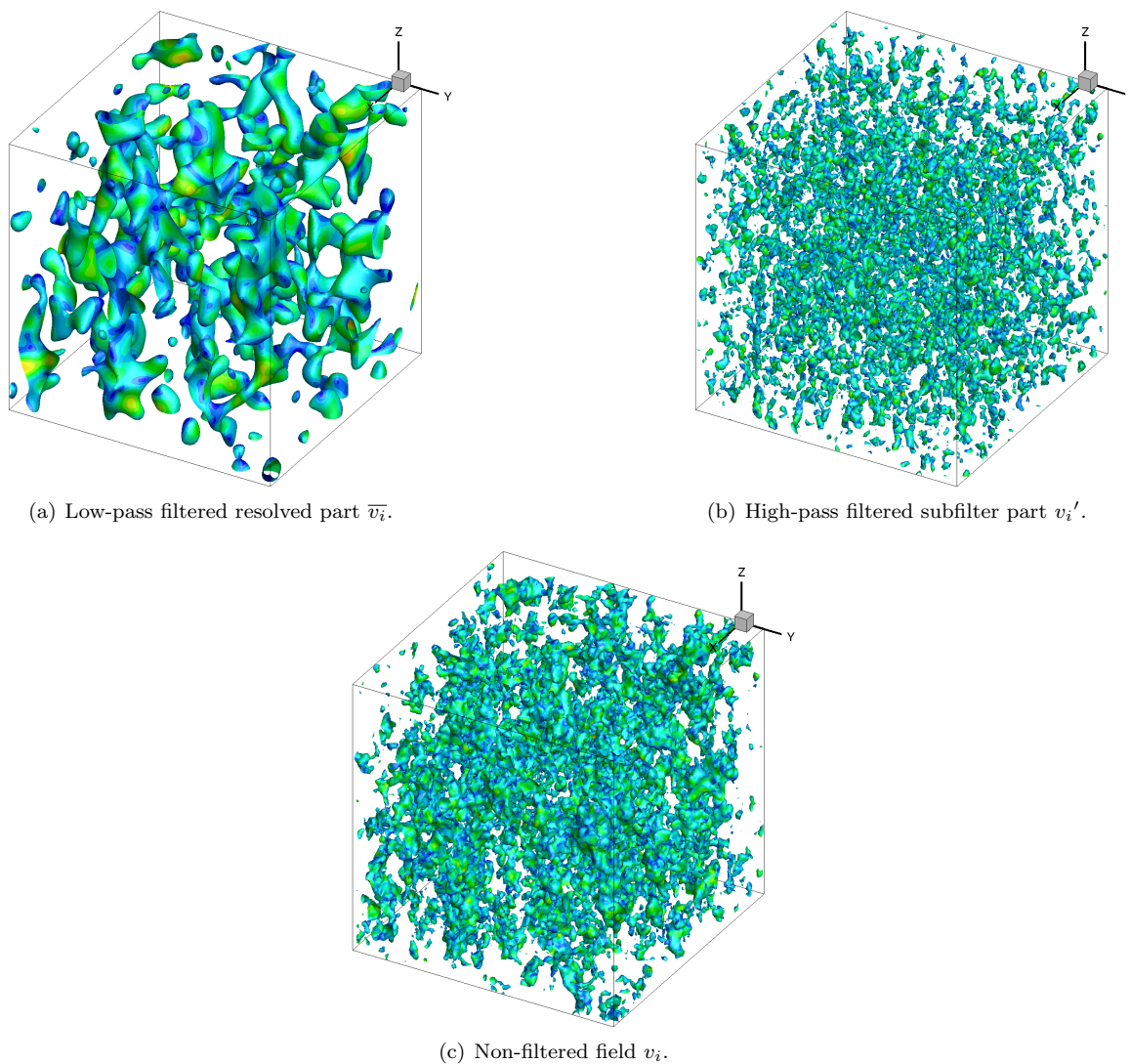
1. Evaluation of the forcing-spectrum function

(a) Low-pass filtered resolved part $\overline{v_i}$.

(b) High-pass filtered subfilter part v_i'.

(c) Non-filtered field v_i.

Figure 7. Synthetic turbulence fluctuations generated for the analysis of the subfilter forcing term and filtered contribution using a sharp spectral filter; shown are iso-contours of z-velocity; colormap related to vorticity magnitude.

The characteristics of the subfilter forcing function Eq. (5) has been further studied using synthetic turbulence to generate homogeneous isotropic turbulence spectra. The study aims to derive in a first step major characteristics to be realized by the stochastic backscatter forcing model eventually used in applications.

To be precise, the goal is not to model the sub-filter velocities to compute the subfilter forcing function in a real application, which would introduce the stringent resolution requirements for the modeling of the residual scales. Rather, the intention is to derive scaling laws and the characteristic shape of the resulting forcing function that is restricted to the resolved regime. A model for it will introduce no more stringent mesh resolution requirements than those imposed by the resolution of the resolved scales.

For this initial scaling study, the spectra have been generated by filtering a stochastic white-noise field with a specific designed spatial filter that enables the generation of different generic turbulence spectra,

American Institute of Aeronautics and Astronautics

adjustable in terms of turbulent length scales L_f and the power laws in the inertial subrange and below the spectrum maximum. For the present study spectra with asymptotic κ^4 increase for $\kappa \to 0$ and a roll-off with κ^{-2} (Liepmann spectrum), $\kappa^{-5/3}$ (von Kármán spectrum), and $\kappa^{-1.1}$ have been studied.

Two different mesh resolutions, 128^3 and 256^3 of non-dimension edge length 2π have been considered. Fig. 7 shows a snapshot of the generated fields on a 128^3 mesh. Depicted are the unfiltered field v_i and the related resolved and subfilter fields $\widetilde{v}_i$ and v_i', respectively. A sharp spectral filter with adjustable cut-off wave-number is applied. From the synthetically generated velocity fluctuations the energy-spectrum function $E(\kappa)$ is evaluated. A typical outcome of the spectral analysis is shown in Fig. 8 for a von Kármán spectrum with decay $\propto \kappa^{-5/3}$. Note, the spectrum exhibits a final roll-off due to the final mesh resolution involved.

High- and low-pass filtered spectra are also shown in the plot. The cut-off wave number is indicated by the vertical line. Eventually, the explicitly derived resolved and subfilter velocities are used to compute the subfilter forcing function Eq. (5). The procedure provides a vector $\widetilde{\boldsymbol{f}}$ that is processed similarly to the velocity vector, thus

Figure 8. Energy-spectrum function with sharp spectral low- and high-pass filtered contributions and related forcing-spectrum function.

providing the subfilter forcing-spectrum function $F(\kappa)$.

Note, as the subfilter forcing function for real turbulence is partly correlated with the resolved quantities. Hence, its computation from synthetic turbulence does not represent the uncorrelated stochastic part of the subfilter forcing alone, i.e. $\widetilde{f}_i^F$ in Eq. (9).

However, in this work the forcing is applied in the framework of a relaxation model, thus f_i^F is deemed to be represented by the complete subfilter forcing-spectrum function. The final levels of correlation with the left-hand side results from the magnitude of the calibrated relaxation parameter.

The forcing-spectrum function reveals a characteristic shape as discussed in the literature, i.e., an increase with k^4-slope for all wave-numbers up to the cut-off wave-number (Leith 1990,[19] Schumann 1995[6]), refer to Fig. 8. This spectral shape can be found over a wide range of cut-off wave-numbers. This shape, furthermore, is also found for other turbulence spectra with different inertial subrange decay powers. Usage of a cut-off filter with finite slope also effects the shape of the forcing-spectrum roll-off but not the κ^4-branch. With the applied stochastic FRPM method a pretty good approximation to this generic shape can be accomplished.

2. Scaling of the forcing-spectrum function

The evaluation of characteristics of the subfilter forcing from synthetic turbulence can be further used to study the scaling of the forcing variance $\widehat{F} = \left\langle \left(f_i^F\right)^2 \right\rangle$ over different cut-off wave-numbers κ_c. Fig. 9 presents a set of forcing spectra $F(\kappa)$ that results from the variation of the cut-off wave-number. Spectra in red are related to the entire subfilter forcing as defined by Eq. (5), spectra in blue present the spectra of the subfilter Reynolds stresses $\overline{\frac{\partial}{\partial x_i}\left(v_i' v_j'\right)}$ alone. It can be seen that for higher wave-number the subfilter forcing spectrum is dominated from contributions coming from terms $\overline{\frac{\partial}{\partial x_i}\left(\widetilde{v}_i v_j' + v_i' \overline{v_j}\right)}$.

Furthermore, a common envelope of all forcing-spectrum functions is apparent, indicated for both sets by black dashed lines. The integral of the forcing-spectrum function gives its variance,

$$\widehat{F} = 2 \int F(\kappa)\mathrm{d}\kappa. \tag{41}$$

The scaling of the forcing with respect to the cut-off wave-number $\widehat{F}(\kappa_c)$ can be found by according integrating of the forcing-spectrum function related to cut-off wave-number κ_c. The result of numerical integration of the spectra is shown in Fig. 10. The evaluation has been conducted using Liepmann spectra with κ^{-2} decay.

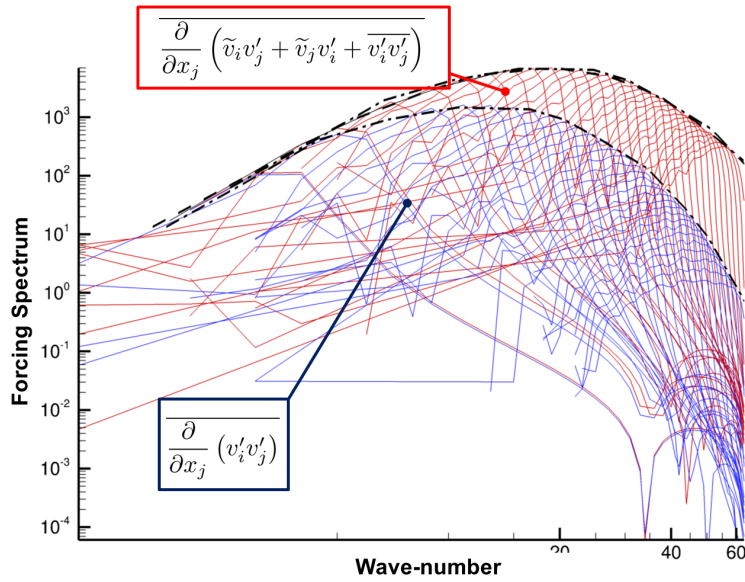American Institute of Aeronautics and Astronautics

Figure 9. Evaluation of the subfilter forcing spectrum for different cut-off wave-numbers; blue, forcing-spectrum function from subfilter Reynolds stresses; red, complete forcing-spectrum function; the data sets reveal a common envelope indicated by the dashed lines.
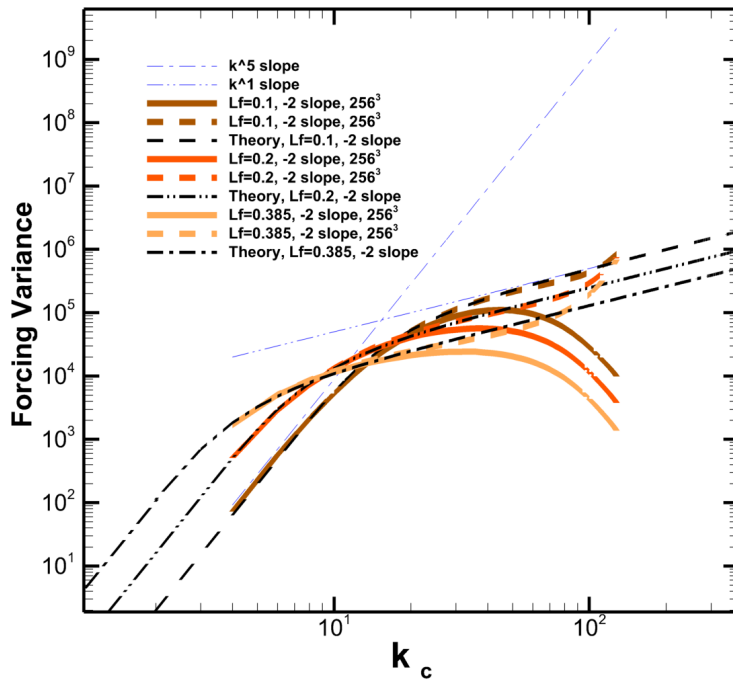

Figure 10. Evaluation of the forcing variance with respect to cut-off wave-number from synthetic turbulence from the integration of numerical evaluated forcing-spectrum functions for 3 different turbulent length scales $L_f = 0.1$, 0.2, and 0.385 and comparison with theory.

Three different integral length scales of the underlying turbulence spectrum are considered, viz, $L_f = 0.1$, 0.2, 0.385. The plot reveals three distinct areas, i.e. an initial increase with slope κ_c^5, followed by a region

with κ_c^1 increase and a final roll-off (colored solid lines). The roll-off is attributed to the limited upper resolution of the generated turbulence spectra. Approximative de-filtering with an inverse Gaussian, shown as colored dashed lines in the plot, reveals a longer coincidence of the curves with an asymptotic κ_c^1 law.

Also shown in the plot are results of a theoretical backscatter variance scaling function derived from Canonical Modeling theory.[34] The theoretical backscatter scaling is derived as

$$\widehat{B}(\lambda_c) = b_1 \mathcal{E}\, g_B\,(\lambda_c) \tag{42}$$

with $\lambda_c := l_c/L_f$, $b_1 \simeq 0.70$ and an analytical given backscatter scaling function

$$g_B\,(\lambda_c) = \lambda_c^{-5} \left\{ 1 - \exp\left(-\left[\frac{5\lambda_c}{2\pi}\right]^2 \right) \left(1 + \left[\frac{5\lambda_c}{2\pi}\right]^2 \right) \right\}. \tag{43}$$

Details of its derivation are beyond the scope of this paper and will be reported elsewhere. The argument of the backscatter scaling function depends on the mesh length scale parameter $l_c = \pi/\kappa_c$. The numerical evaluations reveals the forcing scaling function g_F as defined by Eq. (25). A very good agreement with g_B is observed, which implies direct proportionality,

$$g_B(\lambda_c) \propto g_F(\lambda_c), \tag{44}$$

provided the analytically derived backscatter scaling is substantiated.

Recall, the asymptotic power-law obtained from synthetic turbulence with an increase with $r \simeq 1.0 \ldots 1.33$ in conjunction with the results from the calibration procedure implies a time scale

$$\tau_B \propto \frac{L_f}{\sqrt{k_t}} \left(\frac{l_c}{L_f} \right)^{-p} \tag{45}$$

with $p = 0$, refer to the final calibration discussion. Based on the relation $\widehat{B} = \widehat{F}\tau_B$ derived from the calibration procedure and implied by theoretical reasoning, the agreement of backscatter and forcing scaling function follows inevitably for $p = 0$:

$$g_B \left(\frac{l_c}{L_f} \right) = g_F \left(\frac{l_c}{L_f} \right) \times \left(\frac{l_c}{L_f} \right)^{-p} \overset{p=0}{\rightarrow} g_F \left(\frac{l_c}{L_f} \right). \tag{46}$$

Anyway, the analytical scaling function is very suitable to model the general shape of the forcing variance function, refer to Fig. 11. There, the forcing function variance has been evaluated using integral length scales in the range $L_f = 0.05$ to $L_f = 1.0$ and constant turbulent kinetic energy in the synthetic turbulence realization. The scaling law Eq. (25) implies collapse of all curves if the forcing variance is non-dimensionalized with L_f^2/k_t^2 and plotted over non-dimensional wave-number $L_f\kappa_c$. This is confirmed by the simulations. Because of the limited resolution range obtained with synthetic turbulence, the resolved range differs and, particular, the drop-off of the scaling function from the asymptotic value indicated by the analytical function occurs at different wave-numbers. In (a) the result with 128^3 resolution are shown. In (b) for 256^3 resolution. It is visible that the drop-off occurs at higher wave-numbers for the better resolution.

Note, the analytical scaling function as well as the evaluation shown from synthetic turbulence are based on model spectra with $n = -2$ decay. Analytical scaling functions can be derived for other powers as well. Fig. 12(a) shows analytical scaling functions for $n = -2$ and $n = -1$. Use of a decreased inertial subrange slope causes an increase of the asymptotic power r, following a law $m = 3 + n$. For $n = -5/3$ the power is $m = 4/3$, i.e. renders the value of r as found in the calibration. Note, the increase at low wave-numbers with κ_c^5 is always conserved. The figure also shows a scaling function g_B as suggested by Mason & Thomson,[18] which reveals a similar increase with κ_c^5 at low wave numbers but with zero asymptotic slope.

Note, the analytical scaling function does not include the roll-off of the turbulence spectrum around the Kolmogorov wave-number. This would show up as the behavior indicated by the dashed lines in the diagram, similar to the late behavior seen in the numerical experiment but being caused by physical not numerical reasons.

An increasing forcing function up to the Kolmogorov scale implies significant relevance of backscatter for scale resolving simulation based on truncated scales. The effect of a scale-similar forcing spectrum with a forcing variance increasing with power one is sketched in Fig. 12(b), which implies a constant value of the spectrum maximum. For a specific wave-number κ in the resolved regime this implies reduction of the forcing with increasing cut-off wave-number.
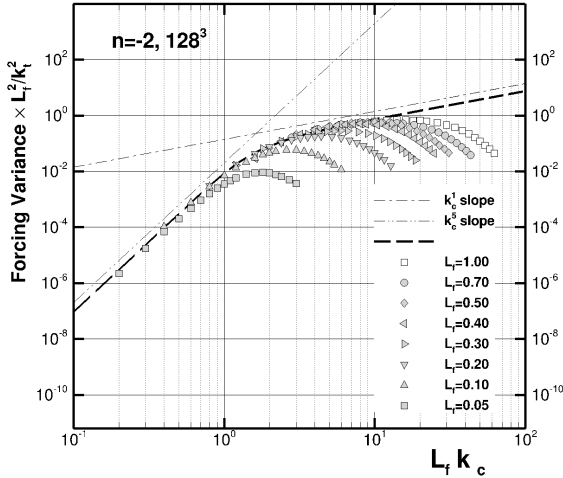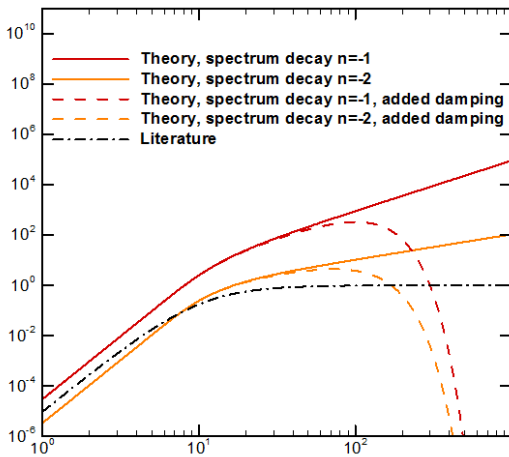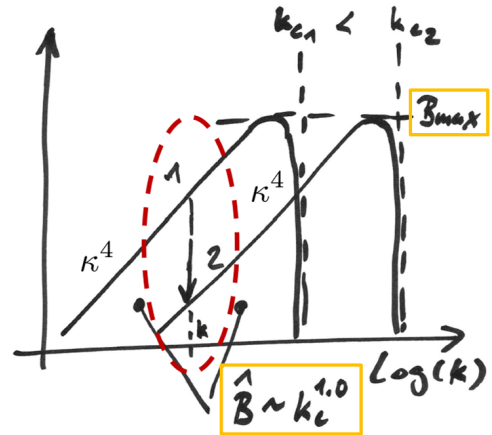
(a) 128^3 mesh.
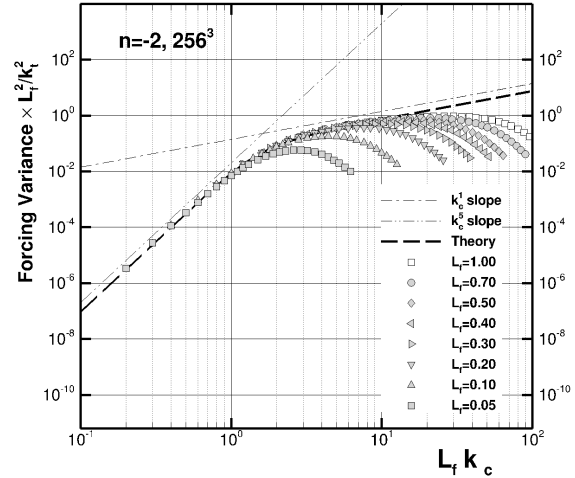
(b) 256^3 mesh.

Figure 11. **Self similarity of the results from synthetic turbulence for turbulent length scales in the range** $L_f = 0.05 \ldots 1.0$ **and comparison with theoretical scaling function.**

(a) Theoretical scaling functions.

(b) Self similar backscatter spectra.

Figure 12. **Left, theoretical scaling functions for** $n = -2$ **and** $n = -1$ **inertial subrange decay and scaling function proposed in literature; right, effect of grid refinement** $\kappa_{c2} > \kappa_{c1}$ **on forcing at wave number** κ.

C.   Concluding remarks

To summarize, the results from DHIT calibration, synthetic turbulence analysis, and theory provide an overall consistent agreement. Fig. 13 depicts the numerical and theoretical derived scaling functions together with 3 data points from forcing calibration, that highlights the general agreement. Finally, the independent calibration of forcing variance and eddy viscosity confirmed validity of the relaxation model ansatz Eq. (10) as a meaningful backscatter model.

American Institute of Aeronautics and Astronautics
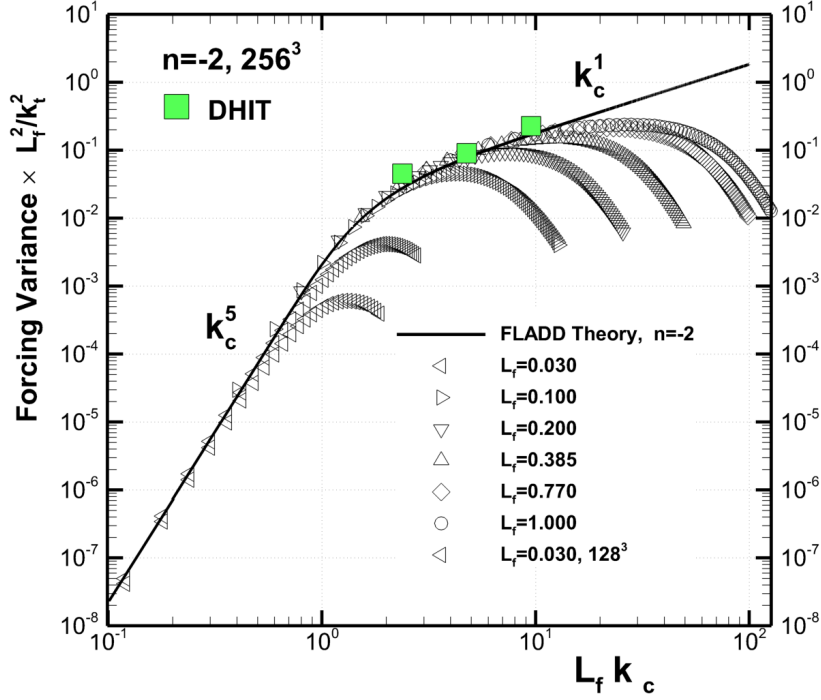
Figure 13. Comparison of numerical and theoretical derived forcing scaling functions with 3 data points from DHIT calibration (squares).

V. Simulation Results

As a first application problem, a generic problem is studied that has been defined in the framework of the EU project JERONIMO. Simulations have been conducted with the above described approach in deterministic (DM) and forced (FES) mode. The configuration consists of a single stream jet (SSJ) in combination with a rectangular unswept wing and NACA0012 wing sections. The nozzle exit Mach number is $M_j = 0.6$ at otherwise static conditions. The NACA0012 airfoil is located parallel to the jet axis at zero degree angle of attack.

The chord length spans four nozzle diameters. The wing trailing edge (TE) is located one nozzle diameter vertically above the jet axis ($H/D_j = 1$) and has an axial displacement of $L/D_j = 4$ from the nozzle exit plane center. A more detailed description of this setup can also be found in Cavalieri et al.[9]

The RANS simulation of the SSJ-NACA0012 wing case is computed with the CFD solver TAU of DLR using a Spalart-Allmares turbulence model. Results of the distributions of Mach number, turbulence kinetic energy, and source variance $\widehat{Q}$ as defined by Eq. (34) are plotted in Fig. 14.

It can be observed in this plot, that the small vertical separation between jet and wing of $\Delta Y = 1D_j$ results in a grazing jet flow along the bottom part of the NACA0012 airfoil.

In order to compute the source variance $\widehat{Q}$, Bradshaw's hypothesis was applied to obtain the turbulence kinetic energy k_t and the dissipation rate ω. Firstly, the shear rate parameter is computed with

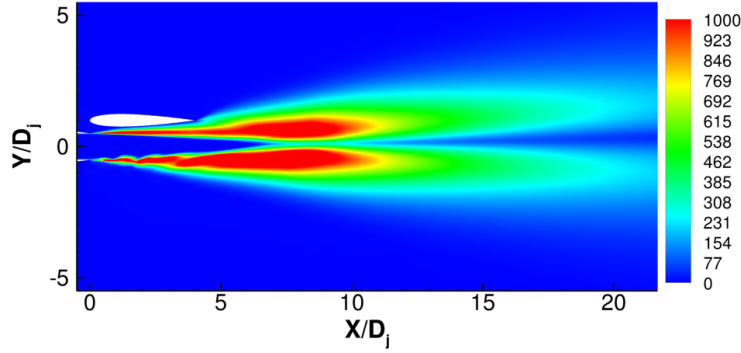$$S^* = \sqrt{2\widetilde{S}_{ij}\widetilde{S}_{ij}}, \tag{47}$$

where the shear rate tensor is given by

$$\widetilde{S}_{ij} = \frac{1}{2}\left(\frac{\partial \widetilde{u}_i}{\partial x_j} + \frac{\partial \widetilde{u}_j}{\partial x_i}\right) - \frac{1}{3}\frac{\partial \widetilde{u}_k}{\partial x_k}\delta_{ij}. \tag{48}$$
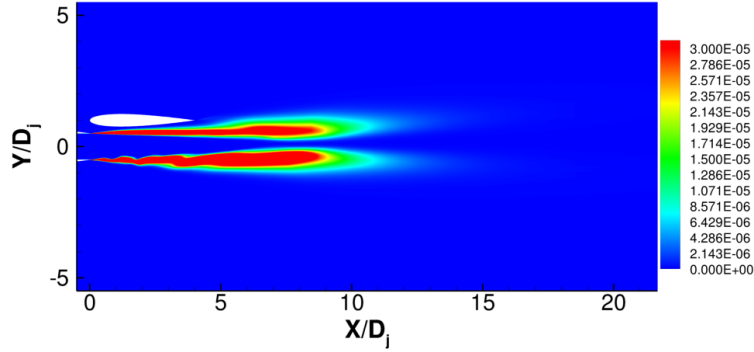
With the obtained shear rate parameter and given eddy viscosity ν_t from RANS, the turbulence kinetic
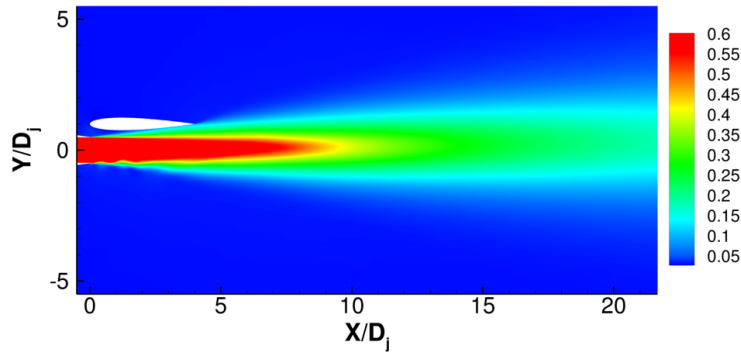
(a) Mach number distribution.

(b) Turbulence kinetic energy.

(c) Source variance distribution $\widehat{Q}$.

Figure 14. RANS results for the configuration with single stream jet and NACA0012 wing in the symmetry plane of the jet at spanwise coordinate $Z/D_j = 0$.

energy (TKE) and dissipation rate are modeled by

$$k_t = \frac{\nu_t S^*}{\sqrt{c_\mu}} \quad \text{and} \quad \omega = \frac{k_t}{\nu_t}. \tag{49}$$

Eventually, turbulent length and times scales are computed from $L_f = c_l/c_\mu \sqrt{k_t}/\omega$ and $\tau_B = c_\tau/c_\mu \omega^{-1}$, with $c_\tau \simeq 0.02$. The grid resolution is derived from $\Delta = \Delta_x$ for the first simulation problem. The grid cut-off length scale is defined by $l_c = 2\Delta$. The resulting distribution of turbulence kinetic energy is shown in Fig. 14(b). Using L_f, l_c, and k_t, evaluation of Eq. (34) provides the distribution as shown in Fig. 14(c).

The above described RANS solution is used subsequently for simulations in deterministic (DM) and forced mode (FES).

For the CAA simulations a CAA mesh is designed based on an H-C topology with 576 grid blocks, which spans a spatial domain in vertical and spanwise direction between $-10 < Y/D_j < 11$ and $-10 < Z/D_j < 10$
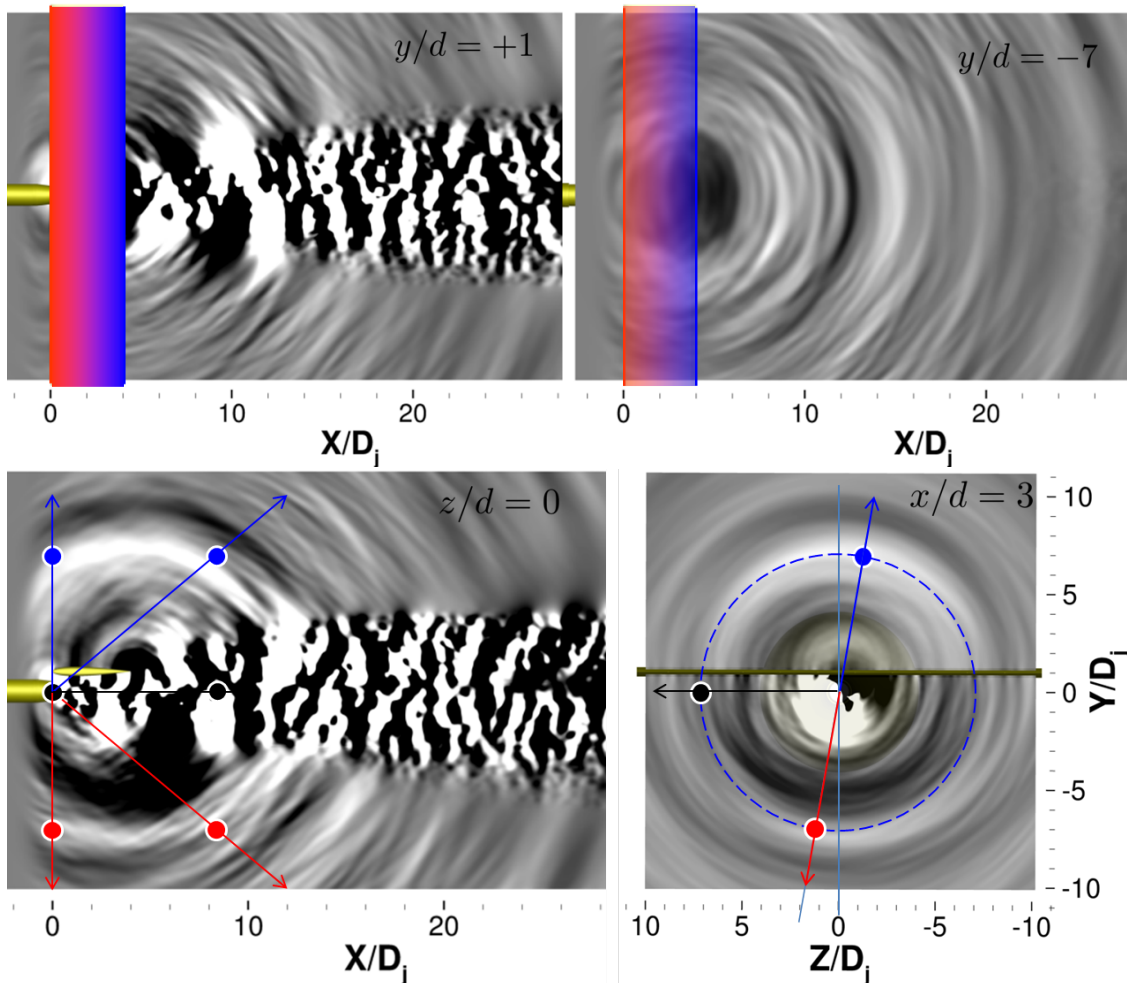
American Institute of Aeronautics and Astronautics

Figure 15. Top-, side- and front-view of the pressure field from FES for a single stream jet in ambient medium ($M_j = 0.6$, $M_\infty = 0.0$, **jet nozzle diameter** $D_j = 0.05m$) **installed at a rectangular wing (trailing edge position** $H/D_j = 1$, $L/D_j = 4$); **microphone positions indicated correspond in color with the spectra shown in Fig. 16.**

with the jet axis located in the center of the computational domain. In axial direction, the CAA domain resolved a domain of $-2.6 < X/D_j < 36$ extension. Sponge layers are defined close to the inflow and outflow regions, reducing the effective CAA domain to $0 < X/D_j < 30$. The total number of mesh points of this CAA mesh is 86 Mio.

The same mesh is applied in both CAA computations utilizing two different relaxation parameters, viz $\sigma = 0.01$ in the first computation with and $\sigma = 10^{-4}$ in the second simulation. The value corresponds in magnitude to that derived for the eddy viscosity ν_R, Eq. (19) in the initial jet region, where values $0.5 \cdot 10^{-4}$ to $2 \cdot 10^{-4}$ are obtained. A constant parameter of same magnitude has been used for the initial test reported here. Simulations with spatial distribution could not be finished in due time and will be reported in ongoing work.

The computational time of this configuration was between 3-7 days with 312 CPUs depending on the time sample length. For the evaluation of spectra, 8 microphone circles are defined at incremental polar angle steps of $\Delta\theta = 10°$ between $\theta = 20$ and $\theta = 90°$. On each circle, 72 microphones with a distance of $R/D_j = 7.15$ to the jet axis are distributed equidistantly as depicted in Fig. 1(a).

Fig. 15 is showing the resulting distribution of sound pressure fluctuations for the computation in forced mode, i.e. with relaxation parameter $\sigma = 10^{-4}$. The top part of the figure presents the $X-Z$-plane at $Y/D_j = 1$, which included the NACA0012 trailing edge, and at $Y/D_j = -7$, which is a position below the jet at a distance approximately corresponding to the sample microphone positions. The bottom left part of this figure is showing a $X-Y$-plane at $Z/D_j = 0$, i.e. the symmetry plane of the jet flow, and the bottom
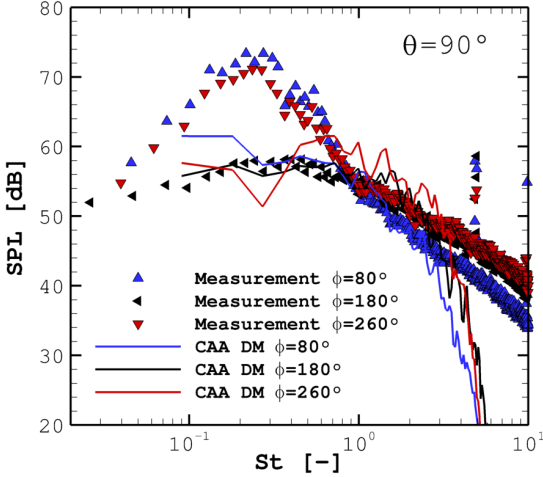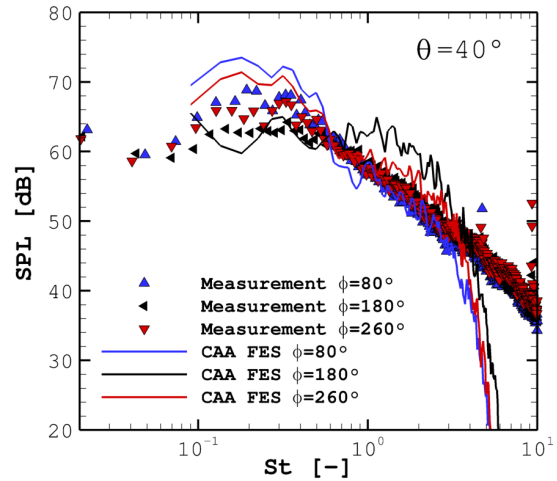
(a) CAA, Deterministic Mode (DM), polar angle $\theta = 90°$.
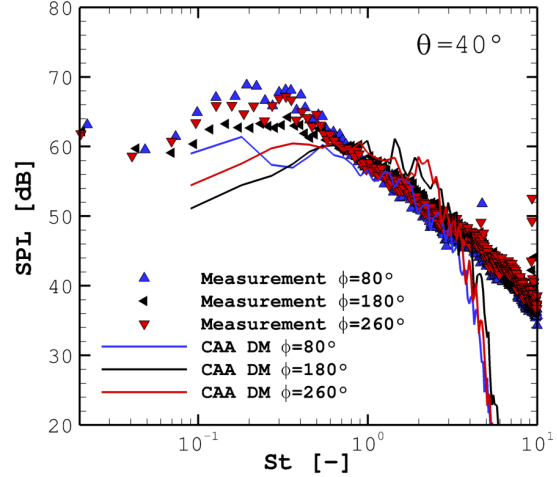
(b) CAA, Deterministic Mode (DM), polar angle $\theta = 40°$.
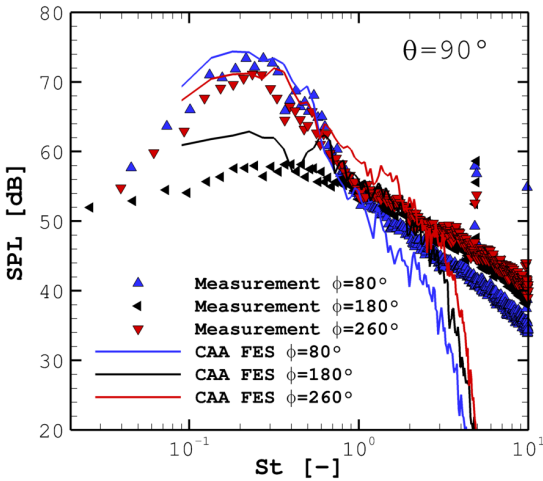
(c) CAA, Forced Eddy Simulation (FES), polar angle $\theta = 90°$.

(d) CAA, Forced Eddy Simulation (FES), polar angle $\theta = 40°$.

Figure 16. Sound pressure level spectra from single stream jet in ambient medium ($M_j = 0.6$, $M_\infty = 0.0$, jet nozzle diameter $D_j = 0.05m$) installed at a rectangular wing (trailing edge position $H/D_j = 1$, $L/D_j = 4$); solid lines: CAA simulation with NACA0012 wing section; symbols, measurement for flat plate wing section;[9] three different azimuthal angles (blue: $\varphi = 80°$, above wing; black: $180°$, spanwise direction; red: $260°$, below wing); polar angle $\theta = 90°$.

right part the $Y - Z$-plane at $Z/D_j = 3$, i.e. a plane cutting the NACA0012 airfoil close before the trailing edge. Six different microphone positions–hereafter used for spectral evaluation–are also illustrated as red, blue and black dots representing the positions at polar angles $\theta = 40°, 90°$ and $\phi = 80°, 180°, 260°$. The plots indicate a strong noise source that causes radiation of circular waves from the trailing edge. This radiation directivity is typically observed for a trailing edge noise source.

The spectra of indicated microphone positions are evaluated in Fig 16 as narrow band spectra for deterministic and forced case. The spectra from Deterministic Mode simulation is plotted in the top row and with Forced Eddy Simulation in the bottom row. For the evaluation of computed spectra the measurements, which are described by Cavalieri et al.[9] for a flat plat wing with same trailing edge position and jet Mach number are used as reference. The measurement as included in these plots (measurement of University of Poitiers, S. Piantanida[43]) is representing the same configuration of a single stream jet with exit Mach number of $Ma_j = 0.6$ and a NACA0012 wing.

American Institute of Aeronautics and Astronautics

As advocated by Cavalieri et al.,[9] the low-frequency hump with its maximum around $St \approx 0.2$ in this setup can be attributed to the interaction of coherent jet structures with the wing trailing edge. Also the CAA results of these computations as shown in the comparison of Fig. 16 are supporting this explanation for the low frequency noise contribution from coherent jet flow structures. Since the forcing parameter in deterministic computation is chosen as a relatively high value, the vortical fluctuation from stochastical modeling are prescribed directly without to resolve larger vortices. Consequently, the jet flow instabilities are not developing for this type of simulation and no low frequency hump is observed in Fig. 16(top) for this case. Otherwise for the forced mode in Fig. 16(bottom), which allows the development of all large scale dynamics including the hydrodynamic instability of the jet flow. In this case, the resolved coherent structures are interacting with the wing trailing edge and result in low frequency contribution that leads to the spectral hump. The comparison of computation in forced mode in Fig. 16(bottom) shows indeed a better agreement in the low frequency range and thus is indicating that the hydrodynamic instability as expected from the measurement is numerically well reproduced.

Furthermore, the Forced Eddy Simulation approach is applied to a more complex configuration (refer to Fig. 1(b),(c)). As the applications discussed in the literature mainly are focused on generic problems such as decaying isotropic turbulence and turbulent channel flows, to the authors knowledge the following simulation presents the most complex case accomplished with an active backscatter model up to date. This constellation consists of an ultra high bypass ratio (UHBR) nozzle ($D_j = 0.16m$ in model scale), which is installed below a high-lift wing with deployed flap and slat (F16 geometry) within the wind tunnel co-flow. The flow conditions are describing the situation at flight approach as defined in the framework of the German national project POWER25.

The RANS solution for this configuration is solved with a two-equation turbulence model (Menter-SST), which provides directly all required quantities for the stochastic modeling. The resolved CAA domain is comprising the entire section of measurement of the AWB[c] wind tunnel. The spatial extensions of the CAA domain are in axial direction $0m < X < 3.5m$, in spanwise direction $-0.4m < y < 0.4m$ and in vertical direction $-1.8m < z < 0.5m$. The box-shaped computational domain is rotated around the y-axis at the nozzle exit to follow the deflection of the jet flow by the wing. The CAA mesh consist of 186 grid blocks with in total 12 Mio. grid points which allows a frequency resolution of around $f_{max} \approx 7kHz$. For this problem, the grid lenght scale is computed from $\Delta = (\Delta_x \Delta_y \Delta_z)^{1/3}$.

Fig. 17(a),(b) and (c) is illustrates flow structures based on the resulting Q-criterion, which demonstrate the development of large vortical structures as visible for instance in the middle part of jet flow from the view above in Fig. 17(c) The stochastic backscatter region is defined by spatial extension of FRPM patch, which was limited here only to jet flow whereas the shear-layer of windtunnel nozzle is excluded. Thus, only the vortical fluctuations of the UHBR nozzle are visible in these plots. A complete suppression of windtunnel shear-layer fluctuations was however not possible, which are partly visible close to the AWB-nozzle and at the end section of the UHBR jet flow.

The plotted 1/3-octave band spectra of Fig. 17(d) are evaluated for a microphone position below the wing trailing edge at around 5 nozzle diameters distance. The solid red line spectrum represents FES results. The other both spectra are obtained from 2-D CAA computations, whereat the spectrum with the peak at lower frequencies (black symbols) represents a 2-D CAA computation with a jet mixing noise source model and the other (red symbols) the computation with an airframe source model. As can be readily seen, if both 2-D spectra are combined, the total contribution as found in the FES simulation is obtained. Herein, the lower frequency position of the jet noise spectrum can be explained with a large diameter of UHBR nozzle. On the other hand, the airframe noise contributes mainly at high frequencies, which even exceeds the SPL values of jet noise contribution. The simulations are conducted for approach flight condition with a relatively low nozzle exit Mach number.

VI. Summary and Conclusions

A stochastic backscatter model has been introduced that is based on an eddy-relaxation source term that provides a combined model for forcing and dissipation. The relaxation parameter defines the amount of correlation of the subfilter forcing with resolved quantities. Its proper calibration is achieved using decaying homogeneous isotropic turbulence (DHIT). Furthermore, characteristics of the backscatter forcing are analyzed from synthetic turbulence data.

---

[c]Acoustic Windtunnel Braunschweig

The results from DHIT calibration, synthetic turbulence analysis, and theory provide an overall consistent agreement. The result imply that an appropriate backscatter time scale is proportional to the turbulent time scale albeit with a constant smaller than one, but not to an eddy turnover time scale. From synthetic turbulence a scaling of the backscatter forcing variance is found in the inertial subrange that increases with power $1.0 \ldots 1.33$. A theoretical scaling function is introduced that very well matches the trends found from numerical experiment.

Finally, the independent calibration of forcing variance and eddy viscosity confirms the validity of the relaxation model ansatz Eq. (10) showing that the eddy viscosity serves as a common relaxation parameter of forced and resolved quantities.

As first application tests, this work presented results for two different installation noise problems involving a cold jet interacting with a wing. The first jet-wing interaction problem studied is based on a generic static jet interacting with a non-inclined rectangular wing. The second problem deals with a dual-stream nozzle installed at a high-lift wing with deployed flap and slat in wind tunnel flow under approach conditions. For both problems installation noise from the airframe yields higher peak levels than the jet-noise contribution alone. For the first problem, relative to the corresponding jet spectrum a low-frequency narrow-band contribution is observed that can be attributed to coherent jet structures interacting with the airfoil trailing edge. Very good agreement with measured spectra is obtained. The agreement reveals the potential of the described method to properly capture the flow dynamics in the resolved regime. For the second problem a broadband airframe installation contribution to the overall spectrum is predicted with peak frequency above the jet contribution.

VII.   Acknowledgment

References

[1]Liu, N.-S. and Shih, T.-H., " Turbulence Modeling for Very Large-Eddy Simulation," *AIAA Journal*, Vol. 44, No. 4, 2006, pp. 687–697.

[2]Dantinne, G., Jeanmart, H., Winckelmans, G., Legat, V., and Carati, D., "Hyperviscosity and Vorticity-Based Models for Subgrid Scale Modeling," *Applied Scientific Research*, Vol. 59, 1998, pp. 409–420.

[3]Ewert, R., "RPM - the fast Random Particle-Mesh method to realize unsteady turbulent sound sources and velocity fields for CAA applications," *AIAA Pap. 2007-3506*, 2007.

[4]Ewert, R., "Broadband slat noise prediction based on CAA and stochastic sound sources from a fast random particle-mesh (RPM) method," *Computers & Fluids*, Vol. 37, 2008, pp. 369–387.

[5]Ewert, R., Dierke, J., Siebert, J., Neifeld, A., Appel, C., Siefert, M., and Kornow, O., "CAA broadband noise prediction for aeroacoustic design," *Journal of Sound and Vibration*, Vol. 330, No. 17, 2011.

[6]Schumann, U., "Stochastic backscatter of turbulent energy and scalar variance by random subgrid-scale fluxes," *Proc. R. Soc. London*, Vol. A, 1995, pp. 293–318.

[7]Piomelli, U., Cabot, W. H., Moin, P., and Lee, S., "Subgrid-Scale backscatter in turbulent and transitional flows," *Physics of Fluids A*, Vol. 3, No. 7, 1991.

[8]R. Zamansky, I. Vinkovic, M. G., "LES approach coupled with stochastic forcing of subgrid acceleration in a high Reynolds number channel flow," *Journal of Turbulence*, Vol. 11, 2010, pp. 1–18.

[9]Cavalieri, A. V., Jordan, P., R.Wolf, W., and Gervais, Y., "Scattering of wave packets by a flat plate in the vicinity of a turbulent jet," *Journal of Sound and Vibration*, Vol. 333, No. 24, 2014, pp. 6516–6531.

[10]Stewart, I., *17 Equations that changed the world*, PROFILE BOOKS LTD, 2012.

[11]Sagaut, P., *Large Eddy Simulation for Incompressible Flows*, Springer, 1998.

[12]Pope, S., *Turbulent Flows*, Cambridge University Press, 2000.

[13]O'Neill, J., Cai, X.-M., and Kinnersley, R., "A generalised stochastic backscatter model: large-eddy simulation of the neutral surface layer," *Q.J.R. Meteorol. Soc.*, Vol. 141, 2015, pp. 2617–2629.

[14]Westbury, P., Dunn, D., and Morrison, J., "Analysis of a stochastic backscatter model for the large-eddy simulation of wall-bounded flow," *European Journal of Mechanics B*, Vol. Fluids 23, 2004, pp. 737–758.

[15]Leslie, D. and Quarini, G., "The application of turbulence theory to the formulation of subgrid modelling procedures," *J. Fluid Mech.*, Vol. 91, 1979, pp. 65–91.

[16]Chasnov, J., "Simulation of the Kolmogorov inertial-subrange using an improved subgrid model," *Phys. Fluids A*, Vol. 3, 1991, pp. 188–200.

[17]Weinbrecht, S. and Mason, P. J., "Stochastic Backscatter for Cloud-Resolving Models. Part I: Implementation and Testing in a Dry Convective Boundary Layer," *Journal of the Atmospheric Sciences*, Vol. 65, 2008, pp. 123–139.

[18]Mason, P. and Thomson, D., "Stochastic backscatter in large-eddy simulations of boundary layers," *J. Fluid Mech.*, Vol. 242, 1992, pp. 51–78.

[19]Leith, C., "Stochastic backscatter in a subgridscale model: Plane shear mixing layer," *Physics of Fluids A*, Vol. 297, No. 2, 1990, pp. 297–299.

[20]Marstorp, L., Brethouwer, G., and Johansson, A. V., "A stochastic subgrid model with application to turbulent flow and scalar mixing," *Physics of Fluids*, Vol. 19, 2007.

[21]Yakhot, V. and Orszag, S. A., "Renormalization Group Theory of Turbulence," *J. Sci. Comput.*, Vol. 1, 1986, pp. 3–51.

[22]Yakhot, V. and Orszag, S. A., "Renormalization Group and Local Order in Strong Turbulence," *Nuclear Physics B*, Vol. 2, 1987, pp. 417–440.

[23]Smith, L. M. and Woddruff, S. L., "Renormalization-Group Analysis of Turbulence," *Annu. Rev. Fluid Mech.*, Vol. 30, 1998, pp. 275–310.

[24]Zhou, Y., "Classical Closure Theory and Lam's Interpretation of ϵ-RNG," NASA Contractor Report 195061 ICASE Report No. 95-19, 1995.

[25]Lesieur, M., *Turbulence in Fluids*, Springer, 2008.

[26]Orszag, S. A., "Analytical theories of turbulence," *Journal of Fluid Mechanics*, Vol. 42, 1970, pp. 363–386.

[27]and, R. E., "Linear and Non-Linear Perturbation Equations with Relaxation Source Terms for Forced Eddy Simulation of Aeroacoustic Sound Generation," AIAA Paper 2014-3053, 2014.

[28]Tam, C. K. and Kurbatski, K., "Microfluid Dynamics and Acoustics of Resonant Liners," *AIAA Journal*, Vol. 38, No. 8, 2000, pp. 1331–1339.

[29]Tam, C., Kurbatski, K., Ahuja, K., and Jr., R. G., "A numerical and experimental investigation of the dissipation mechanism of resonant acoustic liners," *Journal of Sound and Vibration*, Vol. 245, No. 3, 2001, pp. 545–557.

[30]Tam, C. K. and Ju, H., "Airfoil tones at moderate Reynolds number," *Journal of Fluid Mechanics*, Vol. 690, 2011, pp. 536–570.

[31]Delfs, J., Bauer, M., Ewert, R., Grogger, H., Lummer, M., and Lauke, T., *Numerical simulation of aerodynamic noise with DLR's aeroacoustic code PIANO - PIANO manual version 5.2*, Braunschweig, Germany, 2007.

[32]Tam, C. and Webb, J., "Dispersion-Relation-Preserving Finite Difference Schemes for Computational Acoustics," *Journal of Computational Physics*, Vol. 107, 1993, pp. 262–281.

[33]Ewert, R. and Emunds, R., "CAA Slat Noise Studies Applying Stochastic Sound Sources Based On Solenoidal Digital Filters," AIAA Paper 2005-2862, 2005.

[34]Ewert, R., "Canonical Stochastic Realization of Turbulent Sound Sources via Forced Linear Advection-Diffusion-Dissipation Equation," AIAA Paper 2016-2965, 2016.

[35]Young, I. T. and van Vliet, L. J., "Recursvie implementation of the Gaussian filter," *Signal Processing*, Vol. 44, 1995, pp. 139–151.

[36]Siefert, M. and Ewert, R., "Sweeping Sound Generation in Jets Realized with a Random Particle-Mesh Method," AIAA Paper 2009-3369, 2009.

[37]Purser, R., Wu, W.-S., Parrish, D., and Roberts, N., "Numerical aspects of the application of recursive filters to variational statistical analysis. part i: Spatially homogeneous and isotropic gaussian covariances." *Monthly Weather Review*, Vol. 131, 2003, pp. 15241535.

[38]Purser, R., Wu, W.-S., Parrish, D., and Roberts, N., "Numerical aspects of the application of recursive filters to variational statistical analysis. part ii: Spatially inhomogeneous and ansiotropic general covariances." *Monthly Weather Review*, Vol. 131, 2003, pp. 15361548.

[39]Wray, A., "Test Case for the Validation of Large-Eddy Simulation of Turbulent Flows," Unpublished dns data. available on agard database, ftp://torroja.dmt.upm.es, 1997.

[40]Knacke, T., *Numerische Untersuchung des Geräsches massiv abgelöster Strömung bei grosser Reynoldszahl und kleiner Machzahl*, Doctoral thesis, Institute of Fluid Mechanics and Acoustics (ISTA), University of Berlin, Berlin, Germany, 2014.

[41]Reiche, N., Lummer, M., Ewert, R., Delfs, J. W., and Moghadam, M. A., "Towards high-lift noise from Fast Multipole BEM with anisotropic synthetic turbulence sources." *21st AIAA/CEAS Aeroacoustics Conference, Dallas, United Stated of America.*, 2015, AIAA Pap. 2015-2672.

[42]Reiche, N. and Ewert, R., "Realization of Arbitrary Vorticity Spectra using Generic Stochastic Turbulence," Aiaa paper, 2016.

[43]Piantanida, S., "Experimental data on single stream jet with NACA0012 wing," University of poitiers 2016, personal communication, 2016.
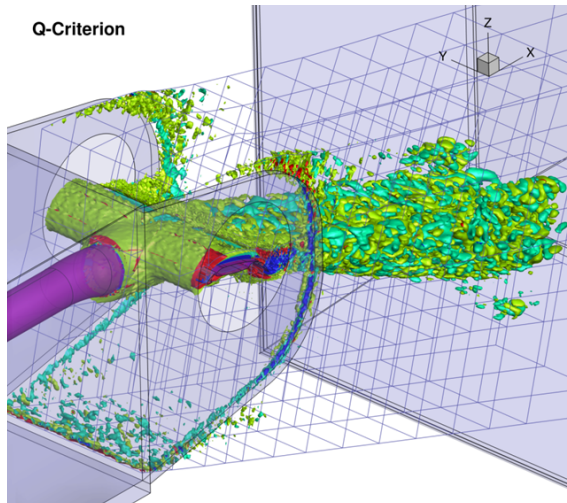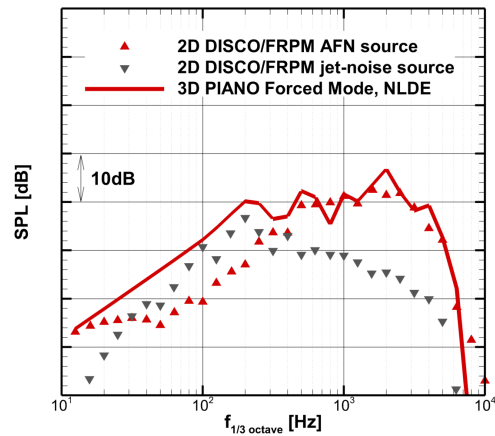
(a) Q-Criterion, FES of AWB set-up.
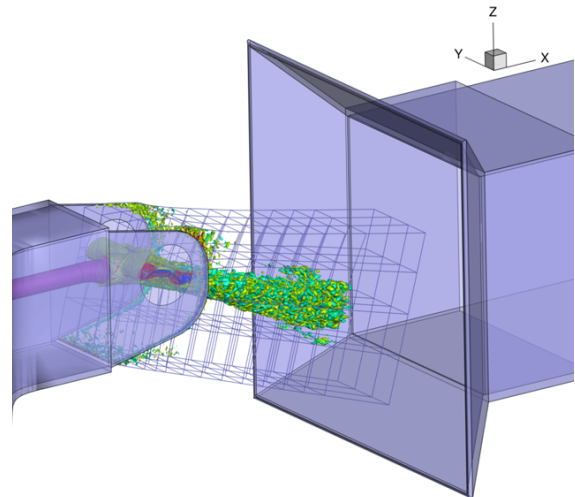
(b) Simulation domain relative to AWB wind tunnel nozzle and collector.
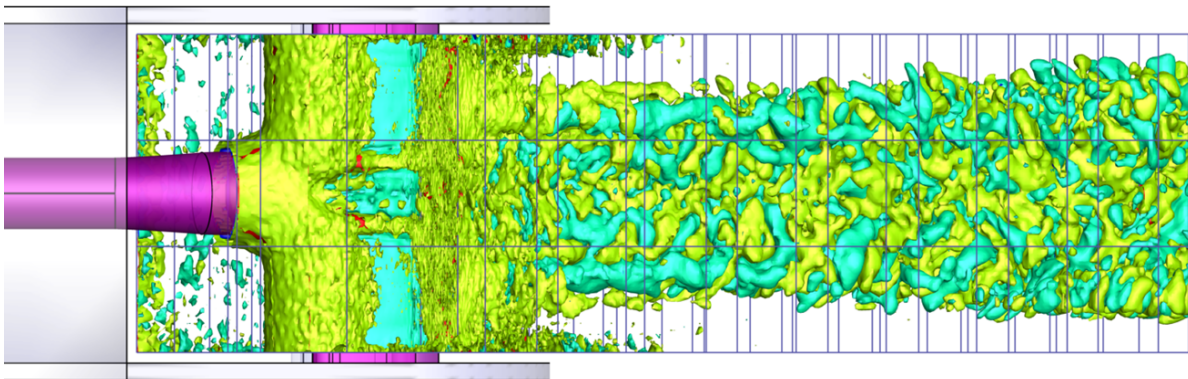
(c) Q-Criterion, view from above.

(d) 1/3-octave spectrum

Figure 17. Simulation of jet-flap interaction noise for a dual-stream nozzle with unswept high-lift wing with slat and flap deployed in the DLR Acoustic Windtunnel AWB; (a)-(c), turbulent structures from FES for the wind tunnel set-up; (d), one-third octave spectrum from 3-D Forced Eddy Simulation (solid line) and individual jet and airframe noise (AFN) spectra from 2-D CAA simulation (symbols).

American Institute of Aeronautics and Astronautics